

Crustal Recycling by Subduction Erosion in the central Mexican Volcanic Belt

Susanne M. Straub^{*1,2}, Arturo Gómez-Tuena³, Ilya N. Bindeman⁴, Louise L. Bolge¹, Philipp A.
Brandl⁵, Ramón Espinasa-Perena⁶, Luigi Solari³, Finlay M. Stuart⁷, Paola Vannucchi⁸ and Georg F.
Zellmer⁹

¹Lamont Doherty Earth Observatory at the Columbia University, 61 Route 9W, Palisades NY 10964,
U.S.A.

²Institute of Earth Sciences, Academia Sinica, 128 Academia Road, Sec. 2, Nankang, Taipei 11529,
Taiwan, ROC

³Centro de Geociencias, Universidad Nacional Autónoma de México, Querétaro 76230, México

⁴Department of Geological Sciences, University of Oregon, Eugene, Oregon, 97403-1272, U.S.A.

⁵Research School of Earth Sciences, Mills Road, The Australian National University, Canberra ACT 0200,
Australia

⁶Centro Nacional de Prevención de Desastres, Secretaría de Gobernación, Av. Delfín Madrigal 665, Col.
Pedregal de Santo Domingo C.P.04360, Delegación Coyoacán, México D.F

⁷Isotope Geosciences Unit, Scottish Universities Research and Reactor Centre, East Kilbride G75 0QF, UK

⁸Department of Earth Sciences, Royal Holloway, University of London Egham, Surrey, TW20 0EX, UK

⁹Institute of Agriculture and Environment, Massey University, Palmerston North 4442, New Zealand

*corresponding author:

e-mail: smstraub@ldeo.columbia.edu

Phone: +845 365 8464

Fax: +845 365 8155

Abstract: 333 words; Text: 10,048 words, 4 Tables, 16 Figures, and Electronic Appendix

revised manuscript, submitted May 2015

34

35 **Abstract**

36 Recycling of upper plate crust in subduction zones, or 'subduction erosion', is a major
37 mechanism of crustal destruction at convergent margins. However, assessing the impact
38 of eroded crust on arc magmas is difficult owing to the compositional similarity between
39 the eroded crust, trench sediment and arc crustal basement that may all contribute to arc
40 magma formation. Here we compare Sr-Nd-Pb-Hf and trace element data of crustal
41 input material to Sr-Nd-Pb-Hf-He-O isotope chemistry of a well-characterized series of
42 olivine-phyric, high-Mg# basalts to dacites in the central Mexican Volcanic Belt (MVB).
43 Basaltic to andesitic magmas crystallize high-Ni olivines that have high mantle-like
44 $^3\text{He}/^4\text{He} = 7\text{--}8 R_a$ and high crustal $\delta^{18}\text{O}_{\text{melt}} = +6.3\text{--}8.5\text{‰}$ implying their host magmas to be
45 near-primary melts from a mantle infiltrated by slab-derived crustal components.
46 Remarkably, their Hf-Nd isotope and Nd/Hf trace element systematics rule out the
47 trench sediment as the recycled crust end member, and imply that the coastal and
48 offshore granodiorites are the dominant recycled crust component. Sr-Nd-Pb-Hf isotope
49 modeling shows that the granodiorites control the highly to moderately incompatible
50 elements in the calc-alkaline arc magmas, together with lesser additions of Pb- and Sr-
51 rich fluids from subducted mid-oceanic ridge basalt (MORB)-type altered oceanic crust
52 (AOC). Nd-Hf mass balance suggests that the granodiorite exceeds the flux of the trench
53 sediment by at least 9-10 times, corresponding to a flux of $\geq 79\text{--}88 \text{ km}^3/\text{km}/\text{Myr}$ into the
54 subduction zone. At an estimated thickness of 1500-1700 m, the granodiorite may
55 buoyantly rise as bulk 'slab diapirs' into the mantle melt region and impose its trace
56 element signature (e.g. Th/La, Nb/Ta) on the prevalent calc-alkaline arc magmas. Deep
57 slab melting and local recycling of other slab components such as oceanic seamounts
58 further diversify the MVB magmas by producing rare, strongly fractionated high-La
59 magmas and a minor population of high-Nb magmas, respectively. Overall, the central
60 MVB magmas inherit their striking geochemical diversity principally from the slab, thus
61 emphasizing the importance of continental crust recycling in modern solid Earth relative
62 to its new formation in modern subduction zones.

63 **1. INTRODUCTION**

64 Subduction zone magmas share remarkable compositional similarities with the
65 continental crust. This has triggered a longstanding and controversial debate regarding
66 whether the continental crust was extracted from the Earth's mantle by processes similar
67 to those of modern convergent margins (e.g. Harrison, 2009; Plank, 2004; Stern, 2011;
68 Taylor, 1967). A pivotal question in this debate is the extent to which subduction

processing can create the typical fractionated trace element signature of the continental crust, or whether this signature is mostly inherited through perpetual recycling of continental crust in subduction zones (e.g. Plank, 2004; Rudnick, 1995). Continental crust is recycled in subduction zones by means of the oceanic sediment subducted at the trenches ('trench sediment') and by subduction erosion of the upper plate crust (Clift and Vannucchi, 2004; Huene and Scholl, 1991). Trench sediment accumulates by surface erosion of the continental crust and resembles average upper continental crust (Plank, 2004; Plank and Langmuir, 1993). Eroded crust is continental crust that is mechanically removed by the subducting slab from forearc basement either by frontal or basal tectonic erosion (Huene et al., 2004; Huene and Scholl, 1991).

Trench sediment recycling has been deduced by the strong compositional links between arc magmas and conjugate trench sediments (e.g. Kay, 1980; Kelemen et al., 2003; Morris et al., 2002; Morris et al., 1990; Plank, 2004; Plank and Langmuir, 1993), and unequivocally confirmed by the detection of cosmogenic ^{10}Be in young arc lavas (Morris et al., 2002; Tera et al., 1986). In contrast, subduction erosion was first recognized from geological observations. For example, uplifted igneous plutonic roots of older arcs may be exposed trenchward to modern arcs which suggests a landward retreat of the trench and forearc crustal removal (Huene and Scholl, 1991; Schaaf et al., 1995). Missing crust is also indicated by vertical fore-arc subsidence without horizontal extension or depression (Huene and Scholl, 1991; Ranero and Huene, 2000). The intensity of subduction erosion may vary considerably through time and among different arc-trench systems (Clift and Vannucchi, 2004; Stern, 2011). On a global scale, mass balance calculations show that subduction erosion accounts for about half (~44-50%) of the crust recycled in subduction zones relative to the trench sediment (~42-56%) (Clift et al., 2009; Scholl and Huene, 2009). Regionally, eroded crust may even exceed the mass of trench sediment by up to a factor of 10 (Vannucchi et al., 2003). Clearly, in view of these numbers, the recycled eroded crust must leave a chemical imprint on the arc that rivals the influence of the recycled trench sediment.

Confirming the recycling of eroded crust in the compositions of arc magmas, however, is a major challenge. The eroded crust mingles with the incoming trench sediment and subducted igneous oceanic basement (AOC, altered oceanic crust), and re-emerges in volcanic arcs together with material from the mantle, and possibly contaminated by the arc's crustal basement. These components must then be distinguished from each other in arc magmas, whereby the eroded crust is similar to trench sediment and arc basement. No unique tracer exists, such as ^{10}Be for oceanic

trench sediment. To add complexity, basal crust from the underside of the upper plate is not accessible, which forestalls direct comparison to arc compositions. Nevertheless, from comprehensive Sr-Nd-Pb-B isotope and trace element studies of arc magmas, evidence for the presence of fore-arc eroded crust has begun to accumulate (e.g. Goss and Kay, 2006; Goss et al., 2013; Holm et al., 2014; Kay et al., 2005; Risse et al., 2013; Tonarini et al., 2011). The common factor of these studies is that they integrate geological and geochemical observations that allow the detection of compositional mismatch between arc chemistry and trench input from the subducted slab that may be reconciled by crust removed from the fore-arc regions.

In the global spectrum of arc magmas, the Mexican margin is a prime setting for tracing the eroded crust in volcanic arcs. First, there is strong evidence for long-term crustal erosion along the Mexican Trench indicated by trench retreat and fore-arc uplift (Clift and Vannucchi, 2004), and by large volumes of missing Mesozoic and Cenozoic crust along the coast (Ducea et al., 2004; Keppie et al., 2012; Morán-Zenteno et al., 1996; Schaaf et al., 1995). Second, the subducted crustal materials - trench sediment, AOC, eroded crust - are obtainable from drill sites at the trench and offshore continental slope as well as from coastal outcrops (exposed Acapulco intrusion, Hernández-Pineda et al., 2011; Watkins and Moore, 1981). Since these crustal materials have distinct compositions, they should be traceable in the arc magmas. Here we report the results of comprehensive comparison between Sr-Nd-Pb-Hf-O-He isotope and trace element data of olivine-bearing arc magmas from the central Mexican Volcanic Belt (MVB) and Sr-Nd-Pb-Hf isotope and trace elements of relevant crustal input materials from the subducting and overlying slab. Our data imply that crust recycled by subduction erosion controls much of the chemistry of the arc magmas erupted in the central MVB.

2. GEOLOGICAL SETTING

The Mexican Volcanic Belt is an active Pliocene-Quaternary volcanic arc that is related to the subduction of the Cocos and Rivera plates along the Middle American Trench (Figure 1) (e.g. Gómez-Tuena et al., 2007b). The trench runs oblique to the arc volcanic front at an angle of $\sim 17^\circ$, because the slab dip decreases eastward and the arc-trench gap widens. In the central MVB, the slab subducts horizontally beneath the forearc and the arc-trench gap measures ~ 360 km (Pardo and Suarez, 1995; Perez-Campos et al., 2008). The study area in central Mexico comprises the monogenetic Sierra Chichinautzin Volcanic Field that is flanked by the composite volcanoes Nevado de Toluca (west) and Popocatepetl (east) (Figure 1, 2). The volcanoes are constructed on a ~ 45 km thick sialic crust of Proterozoic granulites and Mesozoic metapelites, granites and limestones (e.g.

Ortega-Gutiérrez et al., 2012). An extensional crustal stress regime facilitates magma ascent, and mafic and high-Mg# olivine-phyric basalts and andesites are common (Gómez-Tuena et al., 2007b; Schaaf et al., 2005; Wallace and Carmichael, 1999).

Magma compositions in the central MVB range from basalt to dacites which display considerable diversity in trace elements (e.g. Cai et al., 2014; LaGatta, 2003, and references therein; Martinez-Serrano et al., 2004; Schaaf et al., 2005; Siebe et al., 2004a; Straub et al., 2013a; Straub et al., 2014; Wallace and Carmichael, 1999). For petrogenetic studies it was useful to distinguish between a 'basaltic' (olivine-normative) and 'andesitic' (quartz-normative) group, respectively (e.g. Straub et al., 2011b; 2013a; 2014). For the discussion of recycling processes, however, we prefer a division based on the source-sensitive incompatible trace elements (Figure 3). In trace element space, three groups with basaltic and andesitic compositions can be distinguished (see also Appendix A, Figure 1a). The first and far most abundant group (estimated >95 vol% of erupted magmas) are calc-alkaline basalts to dacites (50-67 wt% SiO₂) which construct the voluminous (several 100 km³) composite volcanoes and most of the small-volume (≤1 km³) monogenetic cones. Calc-alkaline magmas combine low Nb = 4-14 ppm abundances with arc-typical strong enrichments of large-ion lithophile elements (LILE) relative to the rare earth elements (REE) and high-field-strength elements (HFSE). The second group ('high-La') consists of light REE (LREE)-enriched basalts to basaltic andesites that have strongly fractionated trace element patterns with strong enrichments in K₂O and LREE, relative depletions in Zr-Hf and steep heavy REE (HREE) patterns. 'High-La' magmas were first described by Gomez-Tuena et al. (2007a) in the Valle de Bravo west of Nevado de Toluca. In the central MVB, only a few high-La magmas erupt from small, monogenetic volcanoes but these magmas are more common in western Mexico (Gomez-Tuena et al., 2011). The third group consists of Nb-rich (>17-36 ppm), mildly alkaline basalts to basaltic andesites (49-57 wt% SiO₂). Nb-rich magmas are enriched in LILE, REE and HFSE, and their trace element pattern resemble those of enriched intraplate basalts (LaGatta, 2003; Schaaf et al., 2005; Straub et al., 2013a; Wallace and Carmichael, 1999). Nb-rich magmas are ubiquitous in the rear-arc region of the MVB, but are rare along the arc volcanic front (e.g. Díaz-Bravo et al., 2014; Gómez-Tuena et al., 2007b; Luhr, 1997).

In the central MVB, Nb-rich magmas erupt from a small, likely coeval group (ca. 1600-1800 year ago, Siebe, 2000; Siebe et al., 2004b; Straub et al., 2013b) of monogenetic volcanoes in the center of the Sierra Chichinautzin, located halfway between Popocatepetl and Nevada de Toluca (Figure 2) (e.g. Straub et al., 2013b; Wallace and

Carmichael, 1999). These Nb-rich magmas are closely associated with the calc-alkaline magmas, erupting from vents only a few kilometers and a few thousands year apart, and even from the same volcano (e.g. Suchiooc, Schaaf et al., 2005; Siebe et al., 2004a; Straub et al., 2013a; Straub et al., 2014). In our sample set, the Nb-rich magmas are over-represented, because they were the target of a more detailed study (Straub et al., 2013a, 2013b).

3. ARC MAGMA PETROGENESIS IN THE CENTRAL MVB

The impact of slab contributions (such as slab fluids, slab partial melts and more recently 'slab diapirs', hereafter summarily referred to as 'slab components') on arc magmas and its consequences for arc petrogenesis and subduction cycling are at the core of arc research (e.g. Gomez-Tuena et al., 2014; Hacker et al., 2011; Plank, 2004). This question is also intensely debated in the central MVB, where much recent progress was made, and for which a short summary is provided here.

The central MVB is constructed on thick continental basement and consequently many studies propose that andesites and dacites evolve from primary basaltic mantle melt by crustal processing (fractional crystallization, crustal assimilation) (e.g. Agustín-Flores et al., 2011; Marquez et al., 1999; Verma, 1999a). However, in recent years evidence has accumulated from several comprehensive petrologic and geochemical studies that the entire range of central MVB basaltic to andesitic (and even dacitic and rhyolitic) magmas are near-primary melts from a subduction-modified mantle that pass the crustal basement nearly unchanged (Gomez-Tuena et al., 2007a; Gómez-Tuena et al., 2008; Straub et al., 2011a; Straub et al., 2013a; Straub et al., 2008). In these models high-Ni olivines with up to 5400 ppm Ni play a key role (Appendix A, Figures 1b,c). These olivines crystallize from basaltic and andesitic magmas and have high $^3\text{He}/^4\text{He}$ ratios of 7-8 R_a which confirms that their host magmas originate in upper mantle. Moreover, the high Ni concentrations in olivine suggests that these magmas are partial melts of secondary olivine-free pyroxenite segregations in the mantle wedge (Straub et al., 2011b). Such segregations formed following the infiltration of silicic components from slab. They melt preferentially relative to the surrounding peridotite in an upwelling mantle and produce a broader range of primary basaltic to dacitic melts that mix variably during ascent to form andesites (Straub et al., 2011a; Straub et al., 2013a; Straub et al., 2008). A major implication of this 'pyroxenite model' is that the central MVB magmas are principally mixtures of slab and mantle materials that underwent little, or negligible, processing in the shallow crust. Thus, the budget of their highly incompatible

trace elements must be strongly controlled by recycled slab materials with little influence of the subarc mantle.

This inference has to date been confirmed by follow-up studies which provided additional insights (e.g. Straub et al., 2013a; 2014). First, the central MVB 'background mantle' (mantle without subduction influence) is highly depleted through serial ('repetitive') melting that is triggered by the continuous hydrous flux from slab since the arc became active in Pliocene. Thus, the mantle wedge is very susceptible to be chemically overprinted by slab additions (2013a; Straub et al., 2008; 2014). The effect of only a few percent melt extraction on the pre-subduction mantle is illustrated in Figure 3, by means of modeling the 'Old Texcal Flow'. This is a monogenetic basalt flow that shows the least slab influence in central Mexico [e.g. lowest SiO₂ ~49 wt%, highest TiO₂ ~2 wt% and lowest Ni in olivines that are only slightly higher than the Ni of olivines in mid-ocean ridge basalts (MORB)], and is considered as best proxy to a melt from the original mantle wedge (Straub et al., 2013a). In incompatible trace elements, the 'Old Texcal Flow' resembles a ~3-4% partial melt of the average primitive mantle (or 'pyrolite') as given by McDonough and Sun (1995) [see Straub (2013a)]. However, the 'Old Texcal Flow' has no end member character in trace element space (Figure 3). While the 'Old Texcal Flow' is per definition a high-Nb basalt (Nb>17 ppm), it has the lowest Nb abundances of this group (Nb=17-19 ppm) and is largely intermediate to calc-alkaline and high-Nb series in other incompatible trace elements (Straub et al., 2014). Therefore, primitive mantle cannot be the prevalent background mantle as it would produce melts that are too enriched in HFSE and light REE for the calc-alkaline series. However, a residual of primitive mantle, produced after only >3-10% melt loss, is highly depleted incompatible elements, and can easily be modified by slab additions (Straub et al., 2014). As discussed previously, in the central MVB, most of the incompatible trace elements (including elements Sr, Nd, Pb and Hf which are associated with isotope tracers) are either exclusively, or substantially contributed from the slab (Straub et al., 2013a; 2014), excepting only Ti and HREE (Ho-Lu).

Second, regardless of the extent of depletion by melting, the Ti and HREE (Ho-Lu) are always controlled by the mantle. In other words, calc-alkaline and high-Nb magmas could contain larger amount of slab material without displaying a garnet signature. Model calculations for REE that use the most recent partitioning data for fluid and/or melt release from slab (Klimm et al., 2008; Skora and Blundy, 2010) show that absorption of up to 30% of slab material would not increasing Ho/Lu of the metasomatized mantle above MORB levels (Straub et al., 2013a; 2014). This amount agrees well with the

'pyroxenite model' that requires a minimum of 15-18% (and likely more) of a silicic slab component in the source in order to convert peridotite to olivine-free pyroxenite (2011b; Straub et al., 2008).

In summary, there is a confluence of evidence for strong slab contributions to the mantle source that may make up several tens of percent of the erupted magmas (2014; Gomez-Tuena et al., 2007a; Straub et al., 2011b; 2013a; 2014). At such proportions, the slab components must control the highly incompatible trace element budgets of the magmas. Moreover, slab components may range from strongly fractionated varieties to components that equally mobilize fluid-mobile LILE, HFSE and LREE. Such diversity - that likely represents heterogeneous slab material rather than an extreme range of fractionation - would be ideal to produce the trace element diversity of calc-alkaline, high-La and Nb-rich series that are so closely associated in time and space. Thus, the central MVB magmas are not only suitable for more detailed investigations of the impact of the slab flux on arc chemistry, but such studies are also a vital test of the prevailing petrogenetic models.

4. SAMPLES AND DATA FOR THIS STUDY

Here we present new $\delta^{18}\text{O}$ data (n=51) for olivine phenocrysts, together with new Hf and Pb isotope ratios of representative bulk rock samples (n= 37 samples). Most of these samples have previously been analyzed for major and trace element abundances, Sr and Nd isotope ratios, and the olivines have been analyzed for composition and $^3\text{He}/^4\text{He}$ (2011b; 2013a; Straub et al., 2008; 2014). In addition, 22 new volcanic rock samples were analyzed for major and trace elements and Sr-Nd-Pb-Hf isotopes, as well as for major element oxide and Ni concentrations of olivines of six samples (Appendix B Tables 1-5). Furthermore, we analyzed up to 22 selected samples of crustal material (xenoliths, basement) for major and trace elements and Sr-Nd-Pb-Hf isotope data (Appendix B Tables 6-9) in order to complement the published data of crustal rocks from the continental basement and offshore central Mexico (Figure 1). All new and previously published data are summarized in Appendix B Table 10.

4.1. Central Mexican arc volcanic rocks

Sample locations for volcanic rocks are shown in Figure 2. Calc-alkaline samples are from many monogenetic volcanoes and two composite volcanoes, Popocatepetl and Toluca. The three high-La basalts and basaltic andesites are from monogenetic volcanoes Yecahuazac Cone, Tuxtepec and St. Cruz. The Nb-rich series are from monogenetic volcanoes Suchiooc, Chichinautzin and Texcal Flow.

4.2. Crustal materials

Crustal materials used in this study include (i) continental crustal basement on which the MVB is constructed, (ii) coastal and offshore crustal basement, and (iii) the terrigenous and pelagic sediment and AOC of the Cocos and Pacific plates (Figure 1).

4.2.1. Continental crustal basement

We obtained new Hf isotope data on crustal xenoliths from Chalcatzingo and Valle de Santiago that have previously characterized for Sr-Nd-Pb isotopes and trace elements by Gómez-Tuena et al. (2008, Chalcatzingo) and Ortega-Gutiérrez et al. (2014, Valle de Santiago). Additional major and trace element data and Sr-Nd-Pb isotope ratios of outcropping crust and crustal xenoliths from within and south of the Mexican Volcanic Belt were compiled from Schaaf et al. (2005, Popocatepetl), Gomez-Tuena et al. (2003; 2008, Teziutlán (Puebla) and Chalcatzingo), Martinez-Serrano et al. (2004, Toluca), Ortega-Gutiérrez et al. (2012; 2014, Puente Negro and Valle Santiago; 2011), and Pérez-Gutiérrez et al. (2009, Xolapa terrane).

4.2.2. Coastal and offshore continental crust

We obtained coastal and offshore continental crust as proxies to crust recycled by crustal erosion. The coastal samples are from the Eocene Acapulco intrusion that is now exposed at the Pacific coast south of the central MVB (Hernández-Pineda et al., 2011). Offshore samples are from DSDP Leg 66 drill sites that recovered biotite gneiss (Site 489) and granodiorite (Site 493) basement southeast of Acapulco (Figure 1). We analyzed Hf isotopes of the Acapulco intrusion [all other data are from Hernández-Pineda et al. (2011)] and major and trace element abundances and Sr-Nd-Pb-Hf isotope ratios of the DSDP basement samples (Appendix B Tables 7-9).

4.2.3. Cocos and Pacific Plates

The crustal compositions of the incoming Cocos Plate are either AOC or oceanic sediment.

4.2.3.1. Pelagic and terrigenous sediment

There are two types of sediment subducted at the trench: (i) the pelagic sediment that accumulated on the Cocos plate, and the (ii) terrigenous (hemipelagic) sediment from the North American plate which covers the continental slope, trench and the near-trench region of the Cocos plate (Watkins and Moore, 1981). The terrigenous sediment reaches a minimum thickness of 625 m on the continental slope, and is still thicker (105 m) than the pelagic sediment (65 m) at the trench Site 487 on the Cocos plate (Figure 1, Watkins et al., 1981). Both sediment types were analyzed for major and trace element abundances

and Sr-Nd-Pb-Hf isotopes by Verma (1999b), LaGatta (2003) and Cai et al. (2014), mainly with samples from DSDP Site 487 on the incoming Cocos plate, supplemented by samples from DSDP Site 488 at the toe of the upper plate continental slope, and from piston cores near the East Pacific Rise (Figure 1). A bulk trench sediment has been calculated (Cai et al., 2014; Plank, 2014).

While not all data were obtained at each site, the two sediment types have clear commonalities and differences. Both types have similar $^{143}\text{Nd}/^{144}\text{Nd}$ ~0.5125 and $^{87}\text{Sr}/^{86}\text{Sr}$ ~0.7085, but the pelagic sediment has higher $^{176}\text{Hf}/^{177}\text{Hf}$ (~0.28294 vs. 0.28278) and Nd/Hf (~20 vs 8) than the terrigenous sediment, and is less radiogenic in Pb isotopes (e.g. $^{206}\text{Pb}/^{204}\text{Pb}$ 18.84 vs 18.52) (Cai et al., 2014; LaGatta, 2003). These differences allow these two lithologies to be traced through the Mexican margin given the sensitivity of arcs towards trench sediment (e.g. Carpentier et al., 2008; Elliott et al., 1997; Plank and Langmuir, 1993).

4.2.3.2. Subducting igneous oceanic crust (AOC)

The subducted AOC has been characterized for trace elements and Sr-Nd-Pb-Hf isotopes using the Miocene basalt basement drilled at DSDP Site 487 on the incoming Cocos Plate (Cai et al., 2014; Verma, 1999b). These data and additional Sr-Nd-Pb-Hf isotope analyses of two Site 487 basement samples (Appendix B Table 7) show that the Site 487 basement resembles depleted zero-age mid-ocean ridge basalts of the East Pacific Rise (PetDB, 2011). Nevertheless, the AOC now beneath the central MVB is about ~5-6 million years older than at the trench, based on the current convergence rate of 47 km/Ma and the arc-trench gap of 360 km (e.g. Manea and Manea, 2011). In order to preclude the possibility of a significant temporal change of the AOC, we analyzed 9 basaltic glasses spanning 10-72 Ma from the western flank of the East Pacific Rise (Pacific Plate), assuming that the crust on both flanks of the East Pacific Rise represents the upwelling mantle. Sample locations are shown in Figure 1 and include DSDP Sites 163, 469, 470 and 472, ODP Sites 1217A, 1243B and IODP Sites 1332, 1333 and 1334. Sr-Nd-Pb-Hf isotope ratios for all sites, and major element oxide abundances for three sites are given in Appendix Tables 8 and 9. The trace element composition of these MORB glasses are from Brandl et al. (2011; 2015).

5. ANALYTICAL METHODS

The majority of the Hf isotope ratios (n=37) were obtained at the Institute for Earth Sciences (IES), Academia Sinica, Taipei, Taiwan on a Nu Plasma using the chemical Hf separation technique after Lee et al. (1999). Additional Sr-Nd-Pb-Hf isotope ratios of

MVB lavas, crustal material and MORB glasses were obtained at Lamont using chemical separation procedures developed by Cai et al. (2014). All trace element data of bulk rocks were obtained by solution ICP-MS methods at the Centro de Geociencias (CGEO), Juriquilla/Qro., Universidad Nacional Autónoma de México, Mexico. Major element oxides were obtained by solution ICP-OES at Lamont. Oxygen isotope data of olivine were obtained at the University of Oregon at Eugene. Olivine major and trace element analyses and major element analyses of MORB glasses were performed at the American Museum of Natural History in New York/USA. Details of analytical methods are given in Appendix B together with the new data (Appendix B Tables 1-9).

6. RESULTS

6.1. O isotopes of the central MVB magmas

The $\delta^{18}\text{O}$ of olivines range from 5.3 to 6.6‰, which corresponds to $\delta^{18}\text{O}_{\text{melt}} = 6.3\text{--}8.4\text{‰}$ of their basaltic and andesite equilibrium melts (Figure 4) (fractionation-correction after, Bindeman, 2008). The $\delta^{18}\text{O}_{\text{oliv}}$ extend to higher values than those reported by Johnson et al. (2009) in young basalts from monogenetic volcanoes in the Michoacan-Guanajuato Volcanic Field farther to the west ($\delta^{18}\text{O}_{\text{oliv}} = 5.5\text{--}6.0\text{‰}$). Together with the olivines of Kluchevskoy volcano, Kamchatka which have $\delta^{18}\text{O}_{\text{oliv}}$ up to 7.6‰ (Auer et al., 2009), central Mexico has the highest $\delta^{18}\text{O}_{\text{oliv}}$ reported in arc magmas worldwide (Martin et al., 2011). Notably, the Nb-rich magmas have similar values and ranges in $\delta^{18}\text{O}_{\text{melt}}$ ($= 7.2 \pm 0.5\text{‰}$, $n=16$) as the calc-alkaline ($\delta^{18}\text{O}_{\text{melt}} = 7.4 \pm 0.5\text{‰}$, $n=24$) and high-La series ($\delta^{18}\text{O}_{\text{melt}} = 6.6\text{--}7.3\text{‰}$, $n=2$). The olivines of the Old Texcal Flow ($\delta^{18}\text{O}_{\text{oliv}} = 5.6\text{‰}$), which best approximates the mantle prior to subduction modification, have one of the lowest melt $\delta^{18}\text{O}_{\text{melt}} = 6.4\text{‰}$ of the MVB. While still slightly above the range of MORB-type mantle melts ($\delta^{18}\text{O}_{\text{melt}} = 5.7 \pm 0.2\text{‰}$, Bindeman, 2008), the data confirm the end member character of the Old Texcal Flow (Straub et al., 2013a).

6.2. Sr-Nd-Pb-Hf isotope ratios

The Sr-Nd-Pb-Hf isotope ratios of our samples are within the range reported from previous studies (e.g. Cai et al., 2014; Martinez-Serrano et al., 2004; Meriggi et al., 2008; Schaaf et al., 2005; Siebe et al., 2004a). Our data, however, illustrate for the first time the systematic differences between calc-alkaline, high-La and Nb-rich magmas in all four isotope systems (Figures 5-7). In Sr-Nd isotope space, the calc-alkaline and high-La magmas are displaced to higher $^{87}\text{Sr}/^{86}\text{Sr}$ and/or higher $^{143}\text{Nd}/^{144}\text{Nd}$ relative to the Nb-rich series (Figure 5). The Old Texcal Flow has the most radiogenic $^{143}\text{Nd}/^{144}\text{Nd}$ and least radiogenic $^{87}\text{Sr}/^{86}\text{Sr}$ closest to Cenozoic MORB which agrees with its end member

character in trace element space (Straub et al., 2013a). In Nd-Hf isotope space, the calc-alkaline and high-La series, and the Nb-rich magmas, respectively, define two parallel, partially overlapping trends along the terrestrial array (Vervoort et al., 2011) (Figure 6) with the calc-alkaline series being displaced towards higher $^{176}\text{Hf}/^{177}\text{Hf}$ at a given $^{143}\text{Nd}/^{144}\text{Nd}$. Again, the Old Texcal Flow has the most radiogenic $^{143}\text{Nd}/^{144}\text{Nd}$ and $^{176}\text{Hf}/^{177}\text{Hf}$ of the central MVB magmas, close in composition to Cenozoic MORB. In Pb isotope space, all arc samples plot on a tight, linear array whereby the Nb-rich series show a displacement towards more radiogenic Pb relative to the calc-alkaline magmas (Figure 7) that is typical for the MVB (Díaz-Bravo et al., 2014; Gomez-Tuena et al., 2007a). However, the Old Texcal Flow does not form the most radiogenic end member, but plots in the middle of the arc array near the transition between calc-alkaline and high-Nb series with a slight, but significant displacement toward higher $^{206}\text{Pb}/^{204}\text{Pb}$.

The Sr-Nd-Pb isotope range of the arc magmas is much more limited than that of the crustal xenoliths which represent the crustal basement (Figure 5). The arc magmas generally align better with potentially recycled crustal components, such trench sediment, AOC, the Acapulco/offshore granodiorites and biotite gneiss which either coincide or bracket the arc array. We note that the relationships between the arc magmas and the recycled components differ in all four isotope systems. For example, in Sr-Nd isotope space, arc magmas are bracketed by AOC and trench sediment, and overlap with the Acapulco/offshore granodiorites, whereas the biotite gneiss is far more enriched than any of these components. In Nd-Hf isotope space, however, the calc-alkaline and high-La arc magmas are instead bracketed by the radiogenic AOC and the unradiogenic granodiorites, respectively, while the trench sediments plots off the arc trend. In this diagram, the Nb-rich magmas extend to slightly more unradiogenic Nd and Hf isotopes than the granodiorites, and the biotite gneiss is far more unradiogenic than any of these compositions. In Pb isotope space, the Cenozoic AOC and the pelagic trench sediment are less radiogenic than the arc magmas, while terrigenous sediment, granodiorites and biotite gneiss are more radiogenic. The granodiorite partially overlaps with the high-Nb series, but not with the calc-alkaline magmas.

7. DISCUSSION

7.1. No evidence for crustal contamination

We emphasize that the new data in their entirety confirm the lack of shallow crustal differentiation in the central MVB magmas (Straub et al., 2011b; 2013a; 2014). As discussed earlier, and exemplified by $^{143}\text{Nd}/^{144}\text{Nd}$ in Figure 8a, the systematic increase of melt silica with radiogenic isotope ratios rules out melt evolution by fractional

crystallization, but links the melt silica increase to changes in source composition (Gomez-Tuena et al., 2007a; Straub et al., 2013a; Straub et al., 2014). Crustal assimilation (or a combination of fractional crystallization and crustal contamination), which is often invoked for such correlations, however, fails in view of the $^3\text{He}/^4\text{He}$ - $\delta^{18}\text{O}$ signature of the high-Ni olivines in the basaltic to andesitic magmas (Figure 4).

The high-Ni, high $^3\text{He}/^4\text{He}$ = 7-8 R_a olivines are either the only or first silicate phase in all three magma series (calc-alkaline, high-La, and high-Nb magmas) (Schaaf et al., 2005; Siebe et al., 2004a; Straub et al., 2008). As early-crystallizing olivines, they retain the primary He-O isotopic signatures of the arc melts before possible later crustal assimilation and secondary alteration (e.g. Eiler et al., 2000; Martelli et al., 2008). The $^3\text{He}/^4\text{He}$ is extremely sensitive towards crustal assimilation, but the high $^3\text{He}/^4\text{He}$ of the olivines does not correlate with melt SiO_2 , despite as little as 0.01% mass of assimilated upper crust would be sufficient to lower the melt $^3\text{He}/^4\text{He}$ below the observed range (Figure 8b). This argues against crustal contamination. On the other hand, the high $\delta^{18}\text{O}_{\text{melt}}$ values of the olivines are clearly above mantle values regardless of the fractionation correction, and point to a crustal component in the melts (Figure 8d,e). While the olivine $\delta^{18}\text{O}$ does not correlate with the average olivine Fo_{78-90} (corresponding to $\text{Mg}\# = 53-74$ of melt) (Figure 9), it increases with increasing SiO_2 of the host melts (Figure 8b). The increase exceeds the $\delta^{18}\text{O}$ increase predicted by fractional crystallization, which agrees with results from high- $\delta^{18}\text{O}$ olivine studies in the western MVB (Johnson et al., 2009). This correlation cannot be attributed to crustal assimilation either, as mixing of a high-Mg#, low SiO_2 , low $\delta^{18}\text{O}$ component (e.g. basaltic mantle melt) with low-Mg#, high SiO_2 , high $\delta^{18}\text{O}$ crustal component predicts correlation of the $\delta^{18}\text{O}$ with both melt SiO_2 and Mg#. Moreover, several tens percent of crustal material would be required in order to reproduce the increase in melt SiO_2 (Figure 8d), which exceeds by far any mass tolerated by the $^3\text{He}/^4\text{He}$ of the olivines. Thus, if there is a crustal component in the central MVB melts, it must have been added from slab. Recycled crustal material, such as trench sediment or eroded crust, is initially rich in radiogenic ^4He and has a low $^3\text{He}/^4\text{He} < 0.1$ (e.g., Martelli et al., 2008), but this He is driven off thermally in the subduction cycle. For one, the highest closure temperature for He in common rock forming minerals is $T_c = 600^\circ\text{C}$ (Martelli et al., 2008). Therefore, subducted crustal ^4He is unlikely to survive the prolonged subduction beneath the Mexican fore-arc, where the slab slowly heats up $>600^\circ\text{C}$ before reaching ca. $700-900^\circ\text{C}$ at arc front depth (e.g. Ferrari et al., 2012; Manea and Manea, 2011). To the other, any remaining crustal He is unlikely to survive heating to temperatures $>700^\circ\text{C}$ during infiltration of the slab material into the hot mantle wedge prior to melt formation.

In summary, there is no evidence of significant crustal contamination in the basaltic and andesitic magmas at least in the olivine crystallization stage. Rather, the olivines crystallize from basaltic to andesitic mantle melts that contain a crustal component from the subducted slab. Remarkably, a correlation between melt silica and $\delta^{18}\text{O}$ is expected from the 'pyroxenite model' of melt-rock reaction that predicts the melt SiO_2 abundance of primary melts to increase with the amount of recycled slab component (e.g. incompatible trace elements, $\delta^{18}\text{O}$) in the mantle source (Straub et al., 2011b; 2014). Here, the melting of secondary pyroxenite veins can create melt series with compositional characteristics reminiscent of fractional crystallization and/or crustal assimilation despite of a different genesis (Straub et al., 2014).

7.2. Identifying recycled slab components in Sr-Nd-Pb-Hf isotope space

7.2.1. Constraints from Sr-Nd-Pb-Hf systematics

The $^3\text{He}/^4\text{He}$ - $\delta^{18}\text{O}$ data constrain the presence of a slab-derived crustal component in the arc magmas, but they do not identify this component which could be AOC, trench sediment or eroded crust, or a mixture of those. This information can be obtained through comparison of arc input and output in Sr-Nd-Pb-Hf isotope and trace element space. To date, studies proposed that the Sr-Nd-Pb-Hf isotope range of the MVB magmas was a mixture of components from the subducted AOC and trench sediment, and mantle wedge (e.g. Cai et al., 2014; Gomez-Tuena et al., 2007a; Straub et al., 2013a; Straub et al., 2014). If this is correct, then mixing trends calculated with these end members must pass through the arc data in Sr-Nd-Pb-Hf isotope space. We tested this inference by calculating first-order mixing curves shown in Figures 5-7. The shape of isotope mixing curves depends only on the isotope and element ratios of the end members, but not the concentrations of the elements (Langmuir et al., 1978). Because AOC (~MORB) and the mantle wedge have similar elemental and - in first approximation - also isotopic ratios, binary mixing curves between AOC and trench sediment are sufficient to test the validity of the AOC-trench sediment-mantle mixing models prior to full quantification. Binary first-order mixing curves were calculated with measured end members given in Table 2.

In Sr-Nd-Pb isotope space, the arc magmas plot on, or reasonably close to, AOC/mantle - trench sediment mixing curves (Figures 5,7). In Pb isotope space, the Cenozoic AOC (average $^{206}\text{Pb}/^{204}\text{Pb}$ ~18.1) is a better fit than the average of zero-age East Pacific Rise MORB which is more radiogenic ($^{206}\text{Pb}/^{204}\text{Pb}$ ~18.4) (PetDB, 2011) (Figure 7). Moreover, the granodiorite and biotite gneiss emerge as possible crustal end member on Sr-Nd-Pb mixing curves, together with the trench sediment. The Sr-Nd-Pb isotopic ratios

do not distinguish between trench sediment and granodiorite/biotite gneiss crustal components. However, this seems possible in Nd-Hf isotope space, because of the different mixing trajectories between AOC/mantle, trench sediment and granodiorite/biotite gneiss. Mixing curves between AOC/mantle, and trench sediment are strongly curved, because these end members have very different Nd/Hf ratios (trench sediment Nd/Hf ~8-20, AOC Nd/Hf ~4, mantle Nd/Hf ~4). Therefore, these curves miss the arc magmas. However, the mixing curves between AOC/mantle and granodiorite are nearly linear and pass through most of the arc data, as the granodiorite and biotite gneiss have a similar low Nd/Hf ~5-7 as the AOC/mantle component. This is confirmed in the corresponding $^{176}\text{Hf}/^{177}\text{Hf}$ vs Nd/Hf diagram, where mixing trends are linear. Again, the mixing lines between AOC/mantle and trench sediment, and particularly AOC/mantle - pelagic trench sediment, clearly miss the bulk of the arc data, while the granodiorite emerges as ideal crustal end member for most of the calc-alkaline/high-La arc magmas, excepting only the Nb-rich magmas which extend to less radiogenic Hf ratios than the granodiorites.

The shape of the AOC-sediment Nd-Hf isotope mixing curves is affected by Nd/Hf fractionation, which may happen during release from slab (e.g. Kessel et al., 2005). Current experimental and observational data disagree on the direction of fractionation. For example, some studies suggest that Nd is preferentially released in slab fluids ($D_{\text{Nd}}/D_{\text{Hf}} < 1$) at pressures of 4 GPa or in a zircon-bearing slab (Kessel et al., 2005; Rubatto and Hermann, 2003). On the other hand, an allanite-saturated slab may preferentially retain Nd relative to Hf at 2.5 to 3 GPa ($D_{\text{Nd}}/D_{\text{Hf}} > 1$) (Klimm et al., 2008; Skora and Blundy, 2010). Therefore, forward models are inconclusive, and we used an inverse approach to test for the possible influence of Nd/Hf fractionation. This is done by varying the Nd/Hf of trench sediment or AOC in a three component mixture (mantle, AOC, sediment) until the Nd-Hf isotope mixing curve passed through the arc data. In short, partial curve fits can be achieved in Nd-Hf isotope space by decreasing the Nd/Hf of the trench sediment or increasing the Nd/Hf of the AOC by a factor of 7 (which is high). However, both solutions fail in the corresponding Nd/Hf vs $^{176}\text{Hf}/^{177}\text{Hf}$ array. Decreasing Nd/Hf of the trench sediment causes the corresponding mixing curves to pass below the arc data in the Nd/Hf vs $^{176}\text{Hf}/^{177}\text{Hf}$ diagram (Figure 10a,b). Increasing Nd/Hf of the AOC, result the corresponding mixing curve plots above the bulk of arc data (Figure 10b,c). The only exception is the high-La group that it could be fit if one of the slab components had a high, fractionated Nd/Hf.

In summary, the Nd-Hf trace element and isotope systematics strongly argue for the granodiorite/biotite gneiss eroded from the forearc as crustal end member in the arc magmas instead of the trench sediment. The granodiorite appears the volumetrically more important recycled lithology, as it seems prevalent in the ubiquitous calc-alkaline series. In contrast, the biotite gneiss is much farther removed from the arc array, and fits lesser well with the arc trends than the granodiorite.

7.2.2. *Other slab components and processes*

While the high-La and Nb-rich series are close to the calc-alkaline magmas in isotope space, their trace element characteristics require additional processes and/or source components. The calc-alkaline and high-La series likely involve the same source materials, but the much higher Nd/Hf of the high-La series (by up to a factor of 3) points to fractionation of these elements which most likely occurs during release from slab. The few high-La magmas do not form trends in Nd-Hf isotope and trace element space and thus provide no clue as which slab component - AOC or granodiorite, or a mixture of both - fractionates. The fractionated nature of this slab component is consistent with their other characteristics, such as the low Nb (=4-8 ppm) which is coupled with high Nb/Ta (17.2-19.5) and LREE-enrichment. Arc magmas with similar signatures are globally rare, but have been reported from the western MVB (Gomez-Tuena et al., 2011) and the Solomon and Indonesia arcs (Goss and Kay, 2009; Koenig and Schuth, 2011; Stolz et al., 1996). In either setting, these magmas have been linked to deep (≥ 140 km) partial melting of an fairly hot (> 900 - 1050°C) eclogitic slab that has residual rutile, but lost all other REE-bearing phases like monazite and allanite (Gomez-Tuena et al., 2011; Koenig and Schuth, 2011). Deep partial slab melts that escaped mingling with other slab component released at shallower depths could account for the isolated eruption of high-La in randomly distributed small ($\ll 1$ km²) cones remote from composite and larger monogenetic volcanoes.

The Nb-rich magmas contain isotopically different source components, as evident from their systematic differences to the calc-alkaline/high-La magmas in Sr-Nd-Pb-Hf space (Figures 10-12). The similarity of the Nb-rich magmas to intraplate magmas has lead to suggestions that these may derive from inherently enriched mantle domains (Cai et al., 2014; Gomez-Tuena et al., 2011; Wallace and Carmichael, 1999). However, their high $\delta^{18}\text{O}$ and high-Ni olivines as well as details of major and trace element systematics (Straub et al., 2013a) clearly point to a slab influence that is comparable in magnitude to that of calc-alkaline series in most of the Nb-rich magmas. Thus, the isotopic differences imply that the mantle sources of the Nb-rich magmas were infiltrated by isotopically

different slab components(s). More than one factor, however, is responsible for the isotopic differences. One factor is that the calc-alkaline/high-La series are more hydrous than the Nb-rich series, having several wt% melt water compared to ≤ 1 wt% of the Nb-rich magmas (e.g. Cervantes and Wallace, 2003a; Johnson et al., 2009; Roberge et al., 2009). Thus, and consistent with previous models (e.g. Gomez-Tuena et al., 2007a; Straub et al., 2014), the source of the calc-alkaline/high-La series seems to receive more slab fluids, such as Sr- and Pb -rich fluids (or possibly hydrous melts) from AOC. An AOC fluid rich in the unradiogenic Pb of the Cenozoic MORB-type crust may shift the calc-alkaline/high-La magmas towards lesser radiogenic Pb isotope ratios relative to the high-Nb magmas in Pb isotope space (Figure 12). AOC fluids may also carry Sr with a $^{87}\text{Sr}/^{86}\text{Sr}$ higher (up to ~ 0.705 , Staudigel et al., 1995) than that fresh MORB ($^{87}\text{Sr}/^{86}\text{Sr} \sim 0.702-3$) of AOC, and shift the calc-alkaline/high-La magmas towards higher $^{87}\text{Sr}/^{86}\text{Sr}$ at a given $^{143}\text{Nd}/^{144}\text{Nd}$ (Figure 11) (e.g. Gomez-Tuena et al., 2007a; 2013a; Straub et al., 2014).

A fractionated fluid component that is enriched in fluid mobile LILE relative to the HFSE does not account for the trace element budget of the Nb-rich magmas. Instead, the slab component infiltrating the source of the Nb-rich magmas must be rich in Nb and Ta, and have high Nb/Ta (16-19.4), high Nb/La (~ 0.9), low Th/La (0.11) and the low Nd/Hf (~ 4). This rules out the granodiorites or similar crustal material as source as this material has fractionated trace element signatures which it would transmit to the mantle (Appendix Figure 2). On the other hand, intraplate basalts have the requisite isotope and trace signatures (e.g. Hofmann, 2003). We tentatively suggest that the source of the high-Nb magmas may have been infiltrated by crust constructed by intraplate seamount magmas. It is possible that such seamount crust was part of the largely inaccessible continental fore-arc basement. Alternatively, it could be part of subducting Cocos plate where clusters of intraplate seamounts are common (e.g. Bohrson and Reid, 1995; Castillo et al., 2010; Niu and Batiza, 1997). Local recycling of seamount material, mingling to some extent with granodiorite, could account for the limited distribution of the Nb-rich magmas in space and time in the Sierra Chichinautzin (Straub et al., 2013b) as well as along the volcanic front of the entire MVB.

7.3. Magnitude and impact of the eroded crust on arc magmas

The granodiorite emerges are important component in the arc magmas. In order to quantitatively assess its influence, we used a combination of inverse methods (trace elements) and forward modeling techniques (radiogenic isotopes). This two-fold approach minimizes the inherent uncertainties of flux quantification where many variables are model-dependent.

7.3.1. *Estimating the total slab flux from trace elements*

First, we estimated the total percentage of slab-derived Sr, Pb, Nd and Hf in the arc magmas by the inverse method of Pearce et al. (1995a). The method calculates the difference for each sample between the observed concentration of an element – which is that of a melt from the subduction-modified mantle - and its concentration in a hypothetical melt from the same mantle free from slab additions ('background mantle'). These differences then scale to the percentage of the slab-derived element in the arc magmas. Assuming Nb and Yb to be mantle-derived, Pearce et al. (1995a) used Nb/Yb ratios to calculate the 'background magma'. In the central MVB, however, Nb is added from slab, and hence TiO_2/Lu is used (Straub et al., 2013a; 2014). Moreover, instead of MORB-type mantle source (Pearce et al., 1995a), we used primitive mantle for calculating the slab-derived percentages for the high-Nb magmas, and residual primitive mantle (after 3.5% melt extraction) calculating those of the calc-alkaline and high-La magmas. Only with magmas with $\text{Mg}\# > 60$ were used in order to ensure the use of trace element ratios in the most primitive magmas.

The trace element inversion confirms a strong slab flux of Sr, Nd, Pb and Hf for all three arc magma series, with the Nb-rich magmas (>44-59% of Sr, Nd, Pb and Hf slab-derived) having about one third less slab contribution than the calc-alkaline (>69-89%) and high-La series (73-96%) (Table 1). In Figure 13, the slab-derived percentages are plotted against the relevant isotopic composition. The Old Texcal Flow is always the least influenced by the slab flux (slab-derived Pb ~18%, Sr ~34% Nd ~16% Hf ~20%) and forms a common point of origin from which the trends of calc-alkaline/high-La and high-Nb magmas diverge towards different slab components. These trends agree with a model of a homogenous mantle that was infiltrated by at least two isotopically distinct slab components. Remarkably, there are no clear trends towards the trench sediment, which confirms its negligible influence on the arc magmas. This is most evident for the arc Sr that must principally originate from recycled AOC and/or granodiorite, without any apparent contribution of sedimentary Sr. Another feature is that none of the arc trends heads towards the same, or the same mix, of slab components in all four isotope systems. This supports the concept of the slab flux being a composite of several individual components that mix in variable proportions.

7.3.2. *Quantifying the slab sources in isotope space*

Forward mixing models in isotope space allow for the estimation of the individual contributions of mantle and slab components to the arc magmas. The first step is to fit mixing curves through the arc data with the appropriate end members (mantle, AOC,

granodiorite/seamounts). A model curve is valid if (i) it passes through the data, and (ii) the modeled elemental ratios reasonably reproduce those of the magmas. We first used the measured elemental ratios of the end members (Table 2). If the mixing curve did not pass through the arc data, then the elemental ratios of the slab-derived end members were modified based on the results from experimental studies.

Suitable mixing curves can be generated in Nd-Hf-Pb isotope space without problem (Figures 10,12). In Sr-Nd isotope space, however, the Sr/Nd of the slab component needs to be adjusted in order to reproduce the high Sr/Nd of the arc magmas (calc-alkaline/high-La series Sr/Nd $\sim 25 \pm 4$; Nb-rich magmas Sr/Nd $\sim 19 \pm 4$). This exceeds those of the main sources (mantle $\sim 12-16$, AOC ~ 12 , granodiorite ~ 9 , intraplate seamounts ~ 13). Mixing curves were fitted by increasing the AOC Sr by a factor of 2.5 for the Nb-rich magmas. For the calc-alkaline series, the Sr flux was increased by a factor of 3 for granodiorite and 4 for AOC. While these adjustments are somewhat arbitrary, they provide a measure of the magnitude of the required Sr excess from slab. The final isotope and elemental ratios of the end members are given in Table 2.

For the calculation of the Sr-Nd-Pb-Hf mixing curves, compositions of idealized, average end member are used (Figures 10-12). While mantle, AOC and granodiorite compositions are reasonably well known (Table 2), the composition of the inferred recycled seamount component is unknown, and therefore its quantification is tentative. For an estimate, we used the Sr, Nd, Pb and Hf abundances of off-axis seamounts with Nb $> 13-46$ ppm from Niu and Batiza (1997), and estimated the isotope ratios of end members from the Sr-Nd-Pb-Hf isotope mixing systematics of the arc magmas.

Two different types of background mantle were chosen: a primitive mantle for the Nb-rich magmas, and a residuum of primitive mantle after 3.5% melt extraction for the calc-alkaline and high-La series (Table 2). The elemental abundances and ratios of the slab components vary considerably depending on whether the slab material is released as bulk component ('slab diapir'), or as partial fluid or melt. Forward estimates are thus inherently uncertain because these depend on a multitude of often poorly known variables (e.g. metamorphic history of slab, partition coefficients, mixing proportions, slab residual mineralogy, thermal structure and composition, physical properties). Again, we choose the simplest approach by using the measured elemental abundances of the end members, with only the abundance adjustment for Sr (Table 2). This approach minimizes the calculated influence of the slab flux on the arc magmas. In addition, mixing proportions were chosen to minimize the contributions of granodiorite. In Sr-Nd-Hf isotope space, the arc data can be reproduced with a slab component composed

of 50% AOC and 50% granodiorites (or seamount material for the high-Nb magmas). The same mixing ratio is valid for the AOC-seamount slab component in Pb isotope space. The granodiorites, however, are so enriched in Pb relative to mantle and AOC that only 10% in the slab component is needed to reproduce the data. A 20% of the composite slab component was mixed with the mantle wedge, which is consistent with major and trace element constrained from previous studies (Straub et al., 2011b; 2013a; 2014). Modeling parameters are given in Table 2, and the results are summarized in Table 3.

In summary, the isotope models suggest (within model uncertainty) a slab flux similar in magnitude to results to that produced by the trace element inversion with the exception of Hf (Tables 1 and 3). Slab-derived percentages are for Sr ~78-96% (compared to 49-95% from trace element inversion), for Pb ~76-86% (59-96% from inversion), for Nd ~76-87% (47-93% from inversion) and for Hf ~75-87% (44-73% from inversion). The significant observation is the high slab contribution relative to that of the mantle wedge, and in particular that of the granodiorite. The granodiorite controls the isotope chemistry of the calc-alkaline magmas/high-La, to which they supply most of the Sr ~73%, Pb ~61%, Nd ~68% and Hf ~87%. Likewise, the purported seamount component makes a strong, but somewhat lesser contribution to the Nb-rich magmas (Sr ~37%, Pb ~54%, Nd ~51% and Hf ~46%) relative to mantle and AOC. The overall contributions of the AOC fluids to the arc magmas are fairly low, with only Sr ~23-42%, Pb ~22-25%, Nd ~21-25% and Hf ~27-28%. Even if contribution of the Pb AOC is likely underestimated, as the model makes no allowance for Pb enrichment in AOC fluids, the moderate influence of AOC-derived Pb on the arc Pb isotope ratios agrees with their lack of isotopic overlap with AOC, which is unlike many other arcs where the influence of AOC components is much stronger (Figures 11, 12) (e.g. Straub and Zellmer, 2012). Overall, the modeling results imply a strong influence of eroded granodiorite on the calc-alkaline and high-La magmas, while the Nb-rich magmas are influenced to similar extent by another slab component (possibly seamounts).

7.4. Why does the trench sediment align with the MVB magmas in Sr-Nd-Pb isotope space?

The Acapulco/offshore granodiorites, possibly complemented by an unknown seamount component, provide an excellent recycled crustal component for the MVB magmas, but the question remains why the trench sediments align so well with the arc magmas in Sr-Nd-Pb isotope space? A simple answer may be that trench sediment and arc magmas are essentially mixtures of the same, or similar, components from

continental crust and MORB. The arc magmas, however, form by mixing of these components in the mantle, whereas the sediments form by mixing on the Earth' surface. Marine sediment is essentially the debris of continental erosion (lithogenic dust, volcanic ash, riverine and hemipelagic input) that is diluted by biogenic components in the oceans (Plank, 2004; Plank and Langmuir, 1998; Vervoort et al., 2011). The sediment $^{87}\text{Sr}/^{86}\text{Sr}$ and $^{143}\text{Nd}/^{144}\text{Nd}$ is controlled by Nd- and Sr-rich debris and dust from the North American continent, and is similar in pelagic and terrigenous sediments. The continental debris also controls the Pb isotope composition of the sediments, but close to mid-ocean ridges the continental signal is overprinted by MORB-type Pb delivered by hydrothermal fluids. Thus, only the terrigenous sediment (Pb = 21 ppm) reflects the Pb isotopes of the continental crust, whereas the Pb-rich pelagic sediment (Pb= 66 ppm LaGatta, 2003) is displaced towards the unradiogenic Pb typical of Cenozoic MORB. In Nd-Hf isotope and trace element space, however, sediment does not align with crust-mantle trends, because of fractionation during transport from the continent. For example, early loss of Hf-rich heavy minerals in rivers (e.g. zircon) increases the Nd/Hf ratio of the suspended load, and hydrothermal fluids may change the Nd and Hf isotope ratios of the continental debris (e.g. Garçon et al., 2013; Garçon et al., 2014; Vervoort et al., 2011). Thus, the Nd-Hf isotope and trace element signature of the continental crust is different from the trench sediment, allowing their signatures to be discriminated in the arc magmas.

7.5. Recycling by slab diapirism – a physical model

7.5.1. *Estimating the amount of eroded recycled crust*

A significant outcome of our study is that the trench sediment does not influence the central MVB arc magmas. However, there is no evidence for sediment accumulation in the trench, and all trench sediment seems to have been subducted (Manea et al., 2003). Consequently, the signal of the trench sediment in the calc-alkaline arc magmas must be concealed by the eroded granodiorite. We estimated the minimum amount of granodiorite needed to conceal the trench sediment from the Nd and Hf fluxes. The volume of the trench sediment is $\sim 8.84 \text{ km}^3/\text{km}/\text{Myr}$, at a convergence rate of 52 km/Myr, thickness of 170 m (Plank, 2014), density of $1370 \text{ kg}/\text{m}^3$ and water content of 59 wt%. Thus, it supplies Nd= $169.3 \text{ g}/\text{km}/\text{Myr}$ and Hf= $10.6 \text{ g}/\text{km}/\text{Myr}$ with an average Nd/Hf =16 [based on Plank (2014)]. A similar thickness of granodiorite with a density of $2700 \text{ kg}/\text{m}^3$ and zero water content would supply Nd= $782.9 \text{ g}/\text{km}/\text{Myr}$ and Hf= $136.0 \text{ g}/\text{km}/\text{Myr}$ with an average Nd/Hf=5.8. Therefore, in order to generate Nd/Hf <6 of the total recycled crustal component, the mass of eroded crust must exceed that of the trench

sediment by at least 9-10 times. This corresponds to a minimum rate of recycled granodiorite of ~79-88.4 km³/Myr.

This estimate exceeds by more than two times the estimate of Ducea et al. (2004) who inferred one-dimensional exhumation rates of 0.18 km/Myr from (U-Th)/He thermochronology of the south central Mexican basement, and estimated ~30 km³/km/Myr crustal loss by subduction during the Miocene. On the other hand, our estimate compares well with the numbers derived from the reconstruction of the shape of the missing Eocene to Miocene fore-arc. The unusual location of the MVB at ~360 km from the trench has been interpreted as the result of a process of slab flattening between middle and late Miocene (Ferrari et al., 1999). Thus, the pre-Miocene arc location is inferred from the configuration of the general Rivera-Cocos subduction, where the arc is ~150 km from the trench in the Jalisco-Colima region, but between 150 and 200 km from the trench in Guatemala. At fore-arc crustal thickness of 20 km (Kim et al., 2010), the crustal loss would be between 20x150km²=3000 km² and 20x200 km²=4000km². Given the ~50 Ma age of batholiths of the Acapulco coast (Hernández-Pineda et al., 2011), and a ~17 Ma start of the MVB volcanic activity (Gómez-Tuena et al., 2007b), this yields an average rate of 60-80 km³/km/Myr for the last in 50 Ma. Thus, our estimate can be considered as realistic.

7.5.2. *Granodiorite recycling by slab diapirism*

The high rate of recycled granodiorite has consequences for the style of mass transfer from slab to wedge. Assuming the subducted granodiorite to be ~9-10 times thicker than trench sediment (= 170 m thick), it would reach a thickness of ~1500-1700 meters. Together with the typical low density of a quartz-feldspar lithology (2700 kg/m³) and the estimated slab temperatures below the arc front of ~700-900°C (Ferrari et al., 2012; Manea and Manea, 2011), these are ideal conditions for buoyant detachment of the granodiorite from slab as 'slab diapirs' without need for slab melting (Behn et al., 2011; Gerya et al., 2004; Gómez-Tuena et al., 2014; Hacker et al., 2011). Such slab diapirs are a highly efficient way to transfer large amounts of slab material into the mantle wedge. Silicic diapirs can react with the peridotite in similar ways as perceived for silicic slab fluids or melts, and form secondary pyroxenites. Importantly, as the granodiorite has similar low average Ho/Lu = 2.5 ± 0.5 as the mantle wedge (Ho/Lu ~2.2), it will not impose a garnet signature on the mantle either.

A recycling cartoon is shown in Figure 14. The granodiorite is depicted to rise buoyantly in the form of diapirs without melting. It may have little intrinsic water, but water could be added from the dewatering AOC, as well as from serpentinite lithologies

from within and below the AOC (e.g. Gómez-Tuena et al., 2014). The granodiorite diapirs dominate by far the slab flux, and are complemented by deep slab melts may form at >140 km and infiltrate the source of the high-La magmas. The high-Nb magmas are tentatively interpreted to be recycled intraplate seamount crust that is entrained into the granodiorite diapirs. All slab components rise into the hot interior of the mantle wedge where they react with the peridotite to form pyroxenite segregations that then melt in the upwelling mantle, and mix during ascent through mantle and crust. The numerous, closely spaced, but compositionally highly diverse small volume monogenetic volcanoes ($\leq 1 \text{ km}^3$) may be the surface expressions of a heterogeneous sub-arc mantle interspersed with pyroxenite veins. On the other hand, a succession of individual slab diapirs channelized at a preferred spot of over a longer period of time (several 100 ka to 1 million years), may ultimately accumulate the eruptive volumes of several 100 km^3 typical of the composite volcanoes (e.g. Gómez-Tuena et al., 2014).

7.6. The impact of subduction erosion on the central MVB magmas

Our recycling model implies that the slab flux controls the budget of the highly incompatible elements in the arc magmas. We tested this inference by means of the incompatible element ratios Th/La and Nb/Ta, that are difficult to fractionate during subduction processing (e.g. Foley et al., 2002; Plank, 2004). Th/La ratios (≈ 0.09 to 0.37) span the global range from the low Th/La (~ 0.05) of the mantle to the high Th/La (~ 0.37) of upper continental crust (e.g. Plank, 2004; Rudnick and Gao, 2002). The range of Nb/Ta (≈ 12.3 -19.5) is similarly broad, and only excludes the rare, superchondritic Nb/Ta >19.9 reported from some arcs (Gomez-Tuena et al., 2011; Koenig and Schuth, 2011; Stolz et al., 1996) (Figure 15).

Mixing relationships with $^{143}\text{Nd}/^{144}\text{Nd}$ confirm that the Th/La and Nb/Ta of the calc-alkaline series is inherited from the inherently heterogeneous granodiorite. The granodiorites form a perfect end member that would buffers the MVB magmas at high $^{143}\text{Nd}/^{144}\text{Nd}$ and at a broader range of Th/La and Nb/Ta. Some granodiorites also have the low Th/La and high Nb/Ta intrinsic to the high-Nb magmas. However, oceanic seamounts have the same characteristics and provide a more likely end member given their isotopic and trace element composition (Figure 15).

The strong influence of the various recycled components on MVB melt chemistry is best evident in Nb vs Nb/Ta space (Figure 16). The Old Texcal Flow (proxy to melt from mantle wedge prior to subduction modification) divides this diagram into four quadrants. The high-La magmas all plot in the upper left quadrant which combines high Nb/Ta >17 with low Nb concentrations typical of a signature of deep melts from eclogitic

slabs with residual rutile (Gomez-Tuena et al., 2011; Koenig and Schuth, 2011). The high-Nb series occupy quadrant II with their combination of high Nb and Nb/Ta being tentatively attributed to the recycling of seamount material. The calc-alkaline magmas (quadrant III), have the low Nb and Nb/Ta (~12-16) typical of continental crust material, here recycled by subduction erosion. Calc-alkaline magmas with these characteristics dominate the entire MVB volcanic front (2014; Gómez-Tuena et al., 2007b). Previous studies linked the low arc Nb/Ta to the partial melting of an amphibole-bearing slab, as amphibole is the only major slab phase that can retain Nb relative to Ta, and produces slab melts with low Nb and Nb/Ta (Foley et al., 2002; Gomez-Tuena et al., 2007a; Gomez-Tuena et al., 2011; Koenig and Schuth, 2011). However, most of the MVB arc front is located >80 km above the slab and thus beyond the amphibole-eclogite transition (Tatsumi and Eggins, 1995). Here, regardless of amphibole stability, recycling of pre-existing continental crust with intrinsically low-Nb/Ta provides a simpler cause for the predominantly low Nb/Ta of MVB magmas.

Likewise, if the granodiorite transmits the high Th/La to the calc-alkaline series, there is no need for additional Th/La fractionation of the magmas, either during slab processing (e.g. Cai et al., 2014) or by shallow crustal differentiation (e.g. Plank, 2004). Additional Th/La fractionation is only needed if all source components had lower Th/La than the arc. While AOC, mantle wedge and average trench sediment all have low Th/La (Cai et al., 2014), the granodiorite ($\text{Th/La}=0.25\pm0.10$) has similar high and variable Th/La as the calc-alkaline arc magmas ($=0.21\pm0.06$). Here, our results support the crustal recycling model of Plank (2004) who proposed that the high Th/La in global arcs is essentially inherited from perpetual recycling of continental crust via the trench sediment (~upper continental crust, Plank and Langmuir, 1998) and expand it to include continental crust recycled by subduction erosion.

There are other compositional features that the calc-alkaline central MVB may inherit from granodiorite. The low Sr/Y ~11 of the granodiorite, regardless of additional Sr from AOC fluids, appears to control the low Sr/Y of the arc magmas (<50). This explains the absence of 'adakitic' high Sr/Y > 50 in the central MVB that has been considered as arc with a 'young and hot' slab prone to melting in previous studies (e.g. Cai et al., 2014; Defant and Drummond, 1990). The granodiorites may also buffer the Ba, Rb, Ba and Pb abundances on the arc to their comparatively low abundances, which are too low if the arc input would be made up AOC and the trench sediment that is highly enriched in these elements (Gomez-Tuena et al., 2007a). Overall, the central MVB poses an excellent example for a volcanic arc that may principally grow by recycling of pre-existing

continental crust rather than through the creation of new arc crust by subduction processing.

8. CONCLUSIONS

The following are the conclusions of this study:

- (1) The Nd-Hf isotope and trace element systematics of central Mexican arc magmas identify granodiorites eroded from the continental fore-arc, and not trench sediment, as the principal recycled component of continental crust.
- (2) The calc-alkaline arc magmas of the central MVB (>95% of the erupted volume) are mixtures of recycled granodiorite, subducted AOC and mantle wedge. Rare, strongly fractionated high-La magmas, and a minor group of Nb-rich magmas, can be linked to deep slab melting, and the local recycled of seamount material, respectively.
- (3) With an estimated mass flux of 79-88 km³/km/Myr, thickness of 1500-1700 m and density of 2700 kg/m³, the eroded granodiorite layer is conducive to the buoyant ascent from slab in form of 'slab diapirs', with no need for slab melting, at the estimated slab temperatures of 700-900°C.
- (4) Th/La, Nb/Ta and other key trace element ratios of the calc-alkaline magmas are inherited from the granodiorite, suggesting that the MVB arc grows by recycling of the continental crust rather than by formation of new continental crust.

9. ACKNOWLEDGEMENTS

Special thanks to Der-Chuen Lee, Wen-Yu Hsu and Kuo-Lung Wang for help with Hf separation and isotope analysis at the Institute of Earth Sciences at Academia Sinica (Taipei/Taiwan), and to Ofelia Pérez-Arvizu for help with isotope and trace element analyses at Lamont and the UNAM Centro de Geociencias/Queretaro, Mexico, and to Charlie Langmuir, Terry Plank and Catherine Chauvel for discussion. Vincente Loreto Becerra, Jesús Valenzuela González, Hermes Samir Herrera Fernández and Sergio Nuño Licona provided valuable support in the field. Yue Cai is thanked for help with isotope separation procedures at Lamont. Catherine Chen, Ellen Knapp, Rose Ramirez and Maggie Sochko assisted with sample preparation. Four anonymous reviewers and Associate Editor Andreas Stracke are thanked for their constructive comments. The IODP Gulf Coast Repository/TX provided the samples from DSDP Leg 66 and IODP Legs 320/321. Support from National Science Foundation grants EAR-07-38707 and EAR-

12-20481, and from National Science Council of Taiwan grants 96-2811-M-001-023 and 98-2811-M-001-052 is gratefully acknowledged.

10. REFERENCES CITED

- Agustín-Flores, J., Siebe, C., Guilbaud, M.N., 2011. Geology and geochemistry of Pelagatos, Cerro del Agua, and Dos Cerros monogenetic volcanoes in the Sierra Chichinautzin Volcanic Field, south of México City. *J Volcanol Geotherm Res* 201 143-162, doi:110.1016/j.jvolgeores.2010.1008.1010.
- Auer, A., Bindeman, I.N., Wallace, P.J., Ponomareva, V., Portnyagin, M., 2009. The origin of hydrous, high- $\delta^{18}\text{O}$ voluminous volcanism: diverse oxygen isotope values and high magmatic water contents within the volcanic record of Klyuchevskoy volcano, Kamchatka, Russia *Contrib Mineral Petrol* 157.
- Behn, M.D., Kelemen, P.B., Hirth, G., Hacker, B.R., Massonne, H.J., 2011. Diapirs as the source of the sediment signature in arc lavas. *Nat Geoscience* 4, doi: 10.1038/NGEO1214.
- Bindeman, I., 2008. Oxygen Isotopes in Mantle and Crustal Magmas as revealed by Single Crystal analysis. *Rev Mineral Geochem* 69, 445-478, doi: 410.2138/rmg.2008.2169.2112.
- Blatter, D.L., Carmichael, I.S.E., Deino, A.L., Renne, P.R., 2001. Neogene volcanism at the front of the central Mexican volcanic belt: basaltic andesites to dacites, with contemporaneous shoshonites and high-TiO₂ lavas. *Geol Soc Am Bull* 113, 1324-1342.
- Bohrson, W.A., Reid, M.R., 1995. Petrogenesis of alkaline basalts from Socorro Island, Mexico: Trace element evidence for contamination of ocean island basalt in the shallow ocean crust *J Geophys Res* 100, 24555-24576.
- Brandl, P.A., Regelous, M., Beier, C., Haase, K.M., 2011. Chemical Evolution of the Oceanic Crust on 103 - 108 Year Timescales, AGU Fall Meeting, San Francisco, pp. T31A-2327.
- Brandl, P.A., Regelous, M., Beier, C., O'Neill, S.C., O, N., Haase, K.M., 2015. The chemical stratigraphy of the extrusive oceanic crust: timescales of magma evolution at mid-ocean ridges. submitted to *Lithos*.
- Cai, Y., 2009. Tracing Upper Mantle Heterogeneities with radiogenic isotopes at the Mexican Volcanic Belt and the Arctic Gakkel Ridge, Graduate School of Art and Philosophy. Columbia University, New York, p. 243p.
- Cai, Y., LaGatta, A., Goldstein, S.L., Langmuir, C.H., Gomez-Tuena, A., Martin del Pozzo, A.L., Carrasco-Nunez, G., 2014. Hafnium isotope evidence for slab melt contributions in hot slab arcs: an example of the Central Mexican Volcanic Belt. *Chem Geol* 377, 45-55, <http://dx.doi.org/10.1016/j.chemgeo.2014.1004.1002>.
- Carpentier, M., Chauvel, C., Mattielli, N., 2008. Pb-Nd isotopic constraints on sedimentary input into the Lesser Antilles arc system. *Earth Planet Sci Lett* 272, 199-211, doi:110.1016/j.epsl.2008.1004.1036.
- Castillo, P.R., Clague, D.A., Davis, A.S., Lonsdale, P.F., 2010. Petrogenesis of Davidson Seamount lavas and its implications for fossil spreading center and intraplate magmatism in the eastern Pacific. *G-cubed* 11, doi: 10.1029/2009GC002992.
- Cervantes, P., Wallace, P.J., 2003a. The role of H₂O in subduction zone magmatism: New insights from melt inclusions in high-Mg basalts from central Mexico. *Geochim Cosmochim Acta* 31, 235-238.

- Clift, P.D., Vannucchi, P., 2004. Controls on Tectonic Accretion versus Erosion in Subduction Zones: Implications for the Origin and Recycling of the Continental Crust *Reviews of Geophysics* 42, RG2001, DOI: 2010.1029/2003RG000127.
- Clift, P.D., Vannucchi, P., Morgan, J.P., 2009. Crustal redistribution, crust–mantle recycling and Phanerozoic evolution of the continental crust. *Earth-Science Reviews* 97, 80–104, doi:110.1016/j.earscirev.2009.1010.1003.
- Defant, M., Drummond, M., 1990. Derivation of some modern arc magmas by melting of young subducted lithosphere. *Nature* 347, 662–665.
- Díaz-Bravo, B.A., Gómez-Tuena, A., Ortega-Obregón, C., Pérez-Arvizu, O., 2014. The origin of intraplate magmatism in the western Trans-Mexican Volcanic Belt. *Geosphere* 10, 340–373, doi:10.1130/GES00976.
- Donnelly, K., Goldstein, S.L., Langmuir, C.H., Spiegelman, M., 2004. Origin of Enriched Ocean Ridge Basalt and Implications for Mantle Dynamics. *Earth Planet Sci Lett* 226, 347–366.
- Ducea, M.N., Valencia, V.A., Shoemaker, S., Reiners, P.W., DeCelles, P.G., Fernanda Campa, M., Moran-Zenteno, D., Ruiz, J., 2004. Rates of sediment recycling beneath the Acapulco trench: Constraints from (U-Th)/He thermochronology. *J Geophys Res* 109, B09404, doi:09410.01029/02004JB003112.
- Eiler, J.M., Crawford, A., Elliott, T., Farelly, m.K.A., Valley, J.W., Stolper, E.M., 2000. Oxygen isotope composition of oceanic-arc lavas. *J Petrol* 41, 229–256.
- Elliott, T., Plank, T., Zindler, A., White, W., Bourdon, B., 1997. Element transport from subducted slab to juvenile crust at the Mariana arc. *J Geophys Res* 102, 14991–15019.
- Farley, K.A., Neroda, E., 1998. Noble gases in the Earth's mantle. *Annu Rev Earth Planet Sci* 26, 189–218.
- Ferrari, L., López-Martínez, M., Aguirre-Díaz, G., Carrasco-Núñez, G., 1999. Space-time patterns of Cenozoic arc volcanism in central Mexico: From the Sierra Madre Occidental to the Mexican Volcanic Belt. *Geochim Cosmochim Acta* 27, 303–306.
- Ferrari, L., Orozco-Esquivel, M.T., Manea, V.C., Manea, M., 2012. The dynamic history of the Trans-Mexican Volcanic Belt and the Mexico subduction zone. *Tectonophysics* 522–523, 122–149, doi:110.1016/j.tecto.2011.1009.1018.
- Foley, S.F., Tiepolo, M., Vannucci, P., 2002. Growth of early continental crust controlled by melting of amphibolite in subduction zones. *Nature* 417, 837–840.
- Garçon, M., Chauvel, C., France-Lanord, C., Huyghe, P., Lave, J., 2013. Continental sedimentary processes decouple Nd and Hf isotopes. *Geochim Cosmochim Acta* 121, 177–195, <http://dx.doi.org/110.1016/j.gca.2013.1007.1027>.
- Garçon, M., Chauvel, C., France-Lanord, C., Limonta, M., Garzanti, E., 2014. Which minerals control the Nd-Hf-Sr-Pb isotopic compositions of river sediments? *Chem Geol* 364, 42–55, <http://dx.doi.org/10.1016/j.chemgeo.2013.1011.1018>.
- GeoMapApp, 2014. Marine Geoscience Data System. <http://www.geomapapp.org/>.
- Gerya, T.V., Yuen, D.A., Sevre, E.O.D., 2004. Dynamical causes for incipient magma chambers above slabs. *Geochim Cosmochim Acta* 32, 89–92, doi:10.1130/G20018.20011.
- Gómez-Tuena, A., Díaz-Bravo, B., Vázquez-Duarte, A., Pérez-Arvizu, O., Laura Mori, L., 2014. Andesite petrogenesis by slab-derived plume pollution of a continental rift, in: Gomez-Tuena, A., Straub, S.M., Zellmer, G.F. (Eds.), *Orogenic Andesite and Crustal Growth*. Geological Society of London Special Publication, London, pp. 65–101, doi 110.1144/SP1385.1144.
- Gomez-Tuena, A., LaGatta, A., Langmuir, C.H., Goldstein, S.L., Ortega-Gutiérrez, F., Carrasco-Nunez, G., 2003. Temporal control of subduction magmatism in the eastern Trans-Mexican Volcanic Belt: Mantle sources, slab contributions, and crustal contamination. *Geochem Geophys Geosys* 8, 8913, doi:8910.1029/2002GC000421.

958 Gomez-Tuena, A., Langmuir, C.H., Goldstein, S.L., Straub, S.M., Ortega-Gutierrez, F., 2007a.
 959 Geochemical Evidence for Slab Melting in the Trans-Mexican Volcanic Belt. *J Petrol* 48, 537-
 960 562, doi:510.1093/petrology/egl1071.
 961 Gomez-Tuena, A., Laura Mori, L., Goldstein, S.L., Perez-Arvizu, O., 2011. Magmatic diversity of
 962 western Mexico as a function of metamorphic transformations in the subducted oceanic plate.
 963 *Geochim Cosmochim Acta* 75 213-241, doi:210.1016/j.gca.2010.1009.1029.
 964 Gómez-Tuena, A., Mori, L., Rincón-Herrera, N.E., Ortega-Gutiérrez, F., Solé, J., Iriondo, A., 2008.
 965 The origin of a primitive trondhjemite from the Trans-Mexican Volcanic Belt and its
 966 implications for the construction of a modern continental arc. *Geochim Cosmochim Acta* 36,
 967 471–474, doi: 410.1130/G24687A.
 968 Gómez-Tuena, A., Orozco-Esquivel, M.T., Ferrari, L., 2007b. Igneous petrogenesis of the Trans-
 969 Mexican Volcanic Belt, in: Alaniz-Álvarez, S.A., Nieto-Samaniego, Á.F. (Eds.), *Geology of*
 970 *México: Celebrating the Centenary of the Geological Society of México: Geological Society of*
 971 *America Special Paper*.
 972 Gomez-Tuena, A., Straub, S.M., Zellmer, G.F., 2014. An introduction to orogenic andesites and
 973 crustal growth in: Gomez-Tuena, A., Straub, S.M., Zellmer, G.F. (Eds.), *Orogenic andesites*
 974 *and crustal growth Geological Society of London, London*, pp. 1-13, doi:10.1144/SP1385.1116
 975 Goss, A.R., Kay, S.M., 2006. Steep REE patterns and enriched Pb isotopes in southern Central
 976 American arc magmas: Evidence for forearc subduction erosion? *Geochem Geophys Geosys* 7,
 977 Q05016, doi:05010.01029/02005GC001163.
 978 Goss, A.R., Kay, S.M., 2009. Extreme high field strength element (HFSE) depletion and near-
 979 chondritic Nb/Ta ratios in Central Andean adakite-like lavas (~28°S, ~68°W). *Earth Planet Sci*
 980 *Lett* 279, 97–109.
 981 Goss, A.R., Mahlburg Kay, S., Mpodozis, C., 2013. Andean adakite-like high-Mg andesites on the
 982 Northern margin of the Chilean-Pampean flat-slab (27-28°S) associated with frontal arc
 983 migration and fore-arc subduction erosion. *J Petrol* 54, 2193-2234,
 984 doi:2110.1093/petrology/egt2044.
 985 Hacker, B.R., Kelemen, P.B., Behn, M.D., 2011. Differentiation of the continental crust by
 986 reamination. *Earth Planet Sci Lett* 307 501-516, doi:510.1016/j.epsl.2011.1005.1024.
 987 Harrison, M.T., 2009. The Hadean Crust: Evidence from >4 Ga Zircons. *Annu Re. Earth Planet Sci*
 988 37, 479-505, doi:410.1146/annurev.earth.031208.100151.
 989 Hernández-Pineda, G.A., Solari, L.A., Gómez-Tuena, A., Méndez-Cárdenas, D.L., Pérez-Arvizu,
 990 O., 2011. Petrogenesis and thermobarometry of the ~50 Ma rapakivi granite-syenite Acapulco
 991 intrusive: Implications for post-Laramide magmatism in southern Mexico. *Geosphere* 7, 1-20,
 992 doi:10.1130/GES00744.00741.
 993 Hofmann, A.W., 2003. Sampling Mantle Heterogeneity through Oceanic Basalts: Isotopes and
 994 Trace Elements, in: Holland, H.D., Turekian, K.K., Carlson, R.W. (Eds.), *Treatise on*
 995 *Geochemistry*. Elsevier, pp. 61-101, ISBN 100-108-043751-043756.
 996 Holm, P.M., Søger, N., Thorup Dyhr, C., Rohde Nielsen, M., 2014. Enrichments of the mantle
 997 sources beneath the Southern Volcanic Zone (Andes) by fluids and melts derived from
 998 abraded upper continental crust. *Contrib Mineral Petrol* 167, 1004, DOI 1010.1007/s00410-
 999 00014-01004-00418.
 1000 Huene, R.v., Ranero, C.R., Vannucchi, P., 2004. Generic model of subduction erosion. *Geochim*
 1001 *Cosmochim Acta* 32, 913-916, doi: 910.1130/G20563.20561.
 1002 Huene, R.v., Scholl, D.W., 1991. Observations at convergent margins concerning sediment
 1003 subduction, subduction erosion, and the growth of continental crust. *Reviews of Geophysics*
 1004 29, 279-316.

1005 Jarosewich, E., Nelen, N., Norberg, J., 1980. Reference samples for electron microprobe analysis.
 1006 Geostandard Newsletter 4 (1), 43-47.
 1007 Johnson, E.R., Wallace, P.J., Delgado-Granados, H., Manea, V.C., Kent, A.J.R., Bindeman, I.N.,
 1008 Donegan, C.S., 2009. Subduction-related volatile recycling and magma generation beneath
 1009 central Mexico: insights from melt inclusions, oxygen isotopes and geodynamic models. *J*
 1010 *Petrol* 50, 1729-1764, doi:1710.1093/petrology/egp1051.
 1011 Kay, R.W., 1980. Volcanic arc magmas: Implications of a melting-mixing model for element
 1012 recycling in the crust-upper mantle system. *Journal of Geology* 88, 497-522.
 1013 Kay, S.M., Godoy, E., Kurtz, A., 2005. Episodic arc migration, crustal thickening, subduction
 1014 erosion, and magmatism in the south-central Andes. *Geol Soc Am Bull* 117, 67-88; doi:
 1015 10.1130/B25431.25431.
 1016 Kelemen, P.B., Yogodzinski, G., Scholl, D.W., 2003. Along-strike Variation in the Aleutian Island
 1017 Arc: Genesis of high-mg# andesite and implication for the continental crust, in: Eiler, J. (Ed.),
 1018 Inside the Subduction Factory. *Amer Geophys Un*, pp. 223-276.
 1019 Keppie, D.F., Hynes, A.J., Lee, J.K.W., Norman, M., 2012. Oligocene-Miocene back-thrusting in
 1020 southern Mexico linked to the rapid subduction erosion of a large forearc block. *Tectonics* 31,
 1021 TC2008, doi:2010.1029/2011TC002976.
 1022 Kessel, R., Schmidt, M.W., Ulmer, P., Pettke, T., 2005. Trace element signature of subduction-zone
 1023 fluids, melts and supercritical liquids at 120-180 km depth. *Nature* 437, 724-727,
 1024 doi:10.1038/nature03971.
 1025 Kim, Y., Clayton, R.W., Jackson, J.M., 2010. Geometry and seismic properties of the subducting
 1026 Cocos plate in central Mexico. *J Geophys Res* 115, doi:10.1029/2009JB006942, 002010.
 1027 Klimm, K., Blundy, J.D., Green, T.H., 2008. Trace element partitioning and accessory phase
 1028 saturation during H₂O-saturated melting of basalt with implications for subduction zone
 1029 chemical fluxes. *J Petrol* 49, 523-553, doi:10.1093/petrology/egn1001.
 1030 Koenig, S., Schuth, S., 2011. Deep melting of old subducted oceanic crust recorded by
 1031 superchondritic Nb/Ta in modern island arc lavas. *Earth Planet Sci Lett* 301, 265-274,
 1032 doi:10.1016/j.epsl.2010.1011.1007.
 1033 LaGatta, A.B., 2003. Arc magma genesis in the Eastern Mexican Volcanic Belt, Department of
 1034 Earth and Environmental Sciences. Columbia University, New York, p. 329.
 1035 Langmuir, C.H., Vocke, R.D.J., Hanson, G.N., Hart, S.R., 1978. A general mixing equation with
 1036 applications to Icelandic basalts. *Earth Planet Sci Lett* 37, 380-392.
 1037 Lee, D.C., Halliday, A.N., Hein, J.R., Burton, K.W., Christensen, J.N., Guenther, D., 1999.
 1038 Hafnium Isotope Stratigraphy of Ferromanganese Crusts. *Science* 285, 1052-1054.
 1039 Luhr, J.F., 1997. Extensional tectonics and the diverse primitive volcanic rocks in the western
 1040 Mexican Volcanic Belt. *Can Mineral* 35, 473-500.
 1041 Manea, M., Manea, V.C., Kostoglodov, V., 2003. Sediment fill in the middle American trench
 1042 inferred from gravity anomalies. *Geofis Int* 42, 603-612.
 1043 Manea, V.C., Manea, M., 2011. Flat-slab thermal structure and evolution beneath central Mexico.
 1044 *Pure Appl Geophys* 168, 1475-1487, doi 1410.1007/s00024-00010-00207-00029.
 1045 Marquez, A., Oyarzun, R., Doblas, M., Verma, S.P., 1999. Alkalic (ocean-island basalt type) and
 1046 calc-alkalic volcanism in the Mexican Volcanic Belt: a case for plume-related and propagating
 1047 rifting in an active margin. *Geochim Cosmochim Acta* 27, 51-54.
 1048 Martelli, M., Nuccio, P.M., Stuart, F.M., Di Liberto, V., Ellam, R.M., 2008. Constraints on mantle
 1049 source and interactions from He-Sr isotope variation in Italian Plio-Quaternary volcanism.
 1050 *Geochem Geophys Geosys* 9, Q02001, doi:02010.01029/02007GC001730.
 1051 Martin, E., Bindeman, I., Grove, T.L., 2011. The origin of high-Mg magmas in Mt Shasta and
 1052 Medicine Lake volcanoes, Cascade Arc (California): higher and lower than mantle oxygen

- isotope signatures attributed to current and past subduction. *Contrib Mineral Petrol* 162, 945-960, doi 10.1007/s00410-00011-00633-00414.
- Martinez-Serrano, R.G., Schaaf, P., Solids-Pichardo, G., Hernandez-Bernal, M.S., Hernandez-Trevino, T., Morales-Contreras, J.J., Macias, J.L., 2004. Sr, Nd and Pb isotope and geochemical data from the Quaternary Nevado the Toluca volcano, a source of recent adakite magmatism, and the Tenango Volcanic Field. *J Volcanol Geotherm Res* 138, 77-110.
- McDonough, W.F., Sun, S.S., 1995. The composition of the Earth. *Chem Geol* 120, 223-253.
- Meriggi, L., Macías, J.L., Tommasini, S., Capra, L., Conticelli, S., 2008. Heterogeneous magmas of the Quaternary Sierra Chichinautzin volcanic field (central Mexico): the role of an amphibole-bearing mantle and magmatic evolution processes. *Revista Mexicana de Ciencias Geológicas* 25, 197-216.
- Morán-Zenteno, D.J., Corona-Chavez, P., Tolson, G., 1996. Uplift and subduction erosion in southwestern Mexico since the Oligocene: pluton geobarometry constraints. *Earth Planet Sci Lett* 141, 51-65, doi: 10.1016/0012-1821X(1996)00067-00062.
- Mori, L., Gómez-Tuena, A., Cai, Y.M., Goldstein, S.L., 2007. Effects of prolonged flat subduction on the Miocene magmatic record of the central Trans-Mexican Volcanic Belt. *Chem Geol* 244 (3-4), 452-473.
- Morris, J.D., Gosse, J., Brachfeld, S., Tera, F., 2002. Cosmogenic Be-10 and the Solid Earth: Studies in Geomagnetism, Subduction Zone Processes, and Active Tectonics, in: Grew, E. (Ed.), *Reviews in Mineralogy*. Mineralogical Society of America, Washington, DC, pp. 207-270.
- Morris, J.D., Leeman, W.P., Tera, F., 1990. The subducted component in island arc lavas: constraints from Be isotopes and B-Be systematics. *Nature* 344, 31-36.
- Muenker, C., Pfaender, J.A., Weyer, S., Buechl, A., Kleine, T., Mezger, K., 2003. Evolution of Planetary Cores and the Earth-Moon System from Nb/Ta Systematics. *Science* 301, 84-87.
- Munker, C., Weyer, S., Scherer, E., Mezger, K., 2001. Separation of high field strength elements (Nb, Ta, Zr, Hf) and Lu from rock samples for MC-ICPMS measurements. *Geochem Geophys Geosys* 2, doi: 10.1029/2001GC000183.
- Niu, Y., Batiza, R., 1997. Trace element evidence from seamounts for recycled oceanic crust in the Eastern Pacific mantle. *Earth Planet Sci Lett* 148, 471-483.
- Nowell, G.M., Kempton, P.D., Noble, S.R., Fitton, J.G., Saunders, A.D., Mahoney, J.J., Taylor, R.N., 1998. High precision Hf isotope measurements of MORB and OIB by thermal ionisation mass spectrometry: insights into the depleted mantle. *Chem Geol* 149 (3-4), 211-233.
- O'Nions, R.K., Oxburgh, E.R., 1988. Helium, volatile fluxes and the development of continental crust. *Earth Planet Sci Lett* 90, 331-347.
- Ortega-Gutiérrez, F., Elías-Herrera, M., Gómez-Tuena, A., Mori, L., Reyes-Salas, M., Macías-Romo, C., Solari, L.A., 2012. Petrology of high-grade crustal xenoliths in the Chalcatzingo Miocene subvolcanic field, southern Mexico: buried basement of the Guerrero-Morelos platform and tectonostratigraphic implications. *Int Geology Review* 54, 1597-1634, <http://dx.doi.org/10.1080/00206814.00202011.00649956>.
- Ortega-Gutiérrez, F., Gómez-Tuena, A., Elías-Herrera, M., Reyes-Salas, M., Macías-Romo, C., 2014. Petrology and geochemistry of the Valle de Santiago lower-crust xenoliths: Young tectonothermal processes beneath the central Trans-Mexican volcanic belt. *Lithosphere* in press, doi: 10.1130/L1317.1131.
- Ortega-Gutiérrez, F., Martiny, B.M., Morán-Zenteno, D.J., Reyes-Salas, A.M., Solé-Viñas, J., 2011. Petrology of very high temperature crustal xenoliths in the Puente Negro intrusion: a sapphire-spinel-bearing Oligocene andesite, Mixteco terrane, southern Mexico. *Revista Mexicana de Ciencias Geológicas* 28, 593-629.

1100 Pardo, M., Suarez, G., 1995. Shape of the subducted Rivera and Cocos plate in southern Mexico:
1101 seismic and tectonic implications. *J Geophys Res* 100, 12357-12373.

1102 Pearce, J.A., Baker, P.E., Harvey, P.K., Luff, I.W., 1995a. Geochemical evidence for subduction
1103 fluxes, mantle melting and fractional crystallization beneath the South Sandwich Island Arc. *J*
1104 *Petrol* 36, 1073-1109.

1105 Perez-Campos, X., Kim, Y.H., Husker, A., Davis, P.M., Clayton, R.W., Iglesias, A., Pacheco, J.F.,
1106 Singh, S.K., Manea, V.C., Gurnis, M., 2008. Horizontal subduction and truncation of the Cocos
1107 Plate beneath central Mexico. *Geophys Res Lett* 35, 18303, doi:18310.11029/12008GL035127.

1108 Pérez-Gutiérrez, R., Solari, L.A., Gómez-Tuena, A., Martens, U., 2009. Mesozoic geologic
1109 evolution of the Xolapa migmatitic complex north of Acapulco, southern Mexico: implications
1110 for paleogeographic reconstructions. *Revista Mexicana de Ciencias Geológicas* 26, 201-221.

1111 PetDB, 2011. Information System for Geochemical Data of Igneous and Metamorphic Rocks from
1112 the Ocean Floor. <http://www.earthchem.org/petdb>.

1113 Pfänder, J.A., Münker, C., Stracke, A., Mezger, K., 2007. Nb/Ta and Zr/Hf in ocean island basalts -
1114 Implications for crust-mantle differentiation and the fate of Niobium. *Earth Planet Sci Lett*
1115 254, 158-172, doi:110.1016/j.epsl.2006.1011.1027.

1116 Pin, C., Briot, D., Bassin, C., Poitrasson, F., 1994. Concomitant separation of strontium and
1117 samarium-neodymium for isotopic analysis in silicate samples, based on specific extraction
1118 chromatography. *Analytica Chimica Acta* 298, 209-217.

1119 Plank, T., 2004. Constraints from Thorium/Lanthanum on Sediment Recycling at Subduction
1120 Zones and the Evolution of the Continents. *J Petrol* doi:10.1093/petrology/egi005, 1-24.

1121 Plank, T., 2014. The Chemical Composition of Subducting Sediments, in: Holland, H., Turekian,
1122 K. (Eds.), *Treatise on Geochemistry* (Second Edition). Elsevier, pp. 607-629.

1123 Plank, T., Langmuir, C.H., 1993. Tracing trace elements from sediment input to volcanic output at
1124 subduction zones. *Nature* 362, 739-743.

1125 Plank, T., Langmuir, C.H., 1998. The geochemical composition of subducting sediment and its
1126 consequences for the crust and the mantle. *Chem Geol* 145, 325-394.

1127 Ranero, C.R., Huene, R.v., 2000. Subduction erosion along the Middle American convergent
1128 margin. *Nature* 404, 748-752.

1129 Risse, A., Trumbull, R.B., Kay, S.M., Coira, B., Romer, R.L., 2013. Multi-stage Evolution of Late
1130 Neogene Mantle-derived Magmas from the Central Andes Back-arc in the Southern Puna
1131 Plateau of Argentina. *J Petrol* 10, 1963-1995, doi:1910.1093/petrology/egt1038.

1132 Roberge, J., Delgado-Granados, H., Wallace, P.J., 2009. Mafic magma recharge supplies high CO₂
1133 and SO₂ gas fluxes from Popocatepetl volcano, Mexico. *Geochim Cosmochim Acta* 37, 107-
1134 110; doi: 110.1130/G25242A.

1135 Rubatto, D., Hermann, J., 2003. Zircon formation during fluid circulation in eclogites (Monviso,
1136 Western Alps): Implications for Zr and Hf budget in subduction zones. *Geochim Cosmochim*
1137 *Acta* 67, 2173-2187, doi:2110.1016/S0016-7037(2102)01321-01322.

1138 Rudnick, R., 1995. Making continental crust. *Nature* 378, 571-578.

1139 Rudnick, R., Gao, S., 2002. Composition of the Continental Crust, in: Rudnick, R.L. (Ed.), *The*
1140 *Crust*. Elsevier-Pergamon, Oxford, pp. 1-64.

1141 Schaaf, P., Morales-Zenteno, D., del Sol Hernandez-Bernal, M., Solis-Pichardo, G., Tolson, G.,
1142 Koehler, H., 1995. Paleogene continental margin truncation in southwestern Mexico:
1143 Geochronological evidence. *Tectonics* 14, 1339-1350.

1144 Schaaf, P., Stimac, J., Siebe, C., Macias, J.L., 2005. Geochemical evidence for mantle origin and
1145 crustal processes in volcanic rocks from Popocatepetl and surrounding monogenetic
1146 volcanoes, central Mexico. *J Petrol* 46, 1243-1282.

1147 Scholl, D.W., Huene, R.v., 2009. Implications of estimated magmatic additions and recycling
 1148 losses at the subduction zones of accretionary (non-collisional) and collisional (suturing)
 1149 orogens, in: Cawood, P.A., Kroener, A. (Eds.), *Earth Accretionary Systems in Space and Time*.
 1150 The Geological Society, Special Publications 2009, London, pp. 105-125, doi:
 1151 110.1144/SP1318.1144.
 1152 Siebe, C., 2000. Age and archaeological implications of Xitle volcano, southwestern Basin of
 1153 Mexico City. *J Volcanol Geotherm Res* 104, 45-64.
 1154 Siebe, C., Rodriguez-Lara, V., Schaaf, P., Abrams, M., 2004a. Geochemistry, Sr-Nd isotope
 1155 composition, and tectonic setting of Holocene Pelado, Guespalapa and Chichinautzin scoria
 1156 cones, south of Mexico City. *J Volcanol Geotherm Res* 130, 197-226.
 1157 Siebe, C., Rodriguez-Lara, V., Schaaf, P., Abrams, M., 2004b. Radiocarbon ages of Holocene
 1158 Pelado, Guespalapa, and Chichinautzin scoria cones, south of Mexico City: implications for
 1159 archeology and future hazards. *Bull Volcanol* 66, 203-225 DOI 210.1007/s00445-00003-00304-z.
 1160 Skora, S., Blundy, J., 2010. High-pressure hydrous phase relations of radiolarian clay and
 1161 implications for the involvement of subducted sediment in arc magmatism. *J Petrol* 51, 2211-
 1162 2243, doi:2210.1093/petrology/egq2054.
 1163 Staudigel, H., Davies, G.R., Hart, S.R., Marchant, K.M., Smith, B.M., 1995. Large scale isotopic Sr,
 1164 Nd and O isotopic anomaly of altered oceanic crust: DSDP/ODP sites 417/418. *Earth Planet Sci*
 1165 *Lett* 130, 169-185.
 1166 Stern, C.R., 2011. Subduction erosion: Rates, mechanisms, and its role in arc magmatism and the
 1167 evolution of the continental crust and mantle. *Gondwana Res* 20, 284-308,
 1168 doi:210.1016/j.gr.2011.1003.1006.
 1169 Stolz, A.J., Jochum, K.P., Spettel, B., Hofmann, A.W., 1996. Fluid- and melt-related enrichment in
 1170 the subarc mantle: Evidence from Nb/Ta variations in island-arc basalts. *Geochim Cosmochim*
 1171 *Acta* 24, 587-590.
 1172 Straub, S.M., Gomez-Tuena, A., Stuart, F.M., Zellmer, G.F., Cai, M.Y., Espinasa-Perena, R., 2011a.
 1173 High-Ni Olivines and the Mantle Origin of Arc Andesites, XXV IUGG General Assembly,
 1174 Melbourne, Australia.
 1175 Straub, S.M., Gomez-Tuena, A., Stuart, F.M., Zellmer, G.F., Espinasa-Perena, R., Cai, M.Y., Iizuka,
 1176 Y., 2011b. Formation of hybrid arc andesites beneath thick continental crust. *Earth Planet Sci*
 1177 *Lett* 303, 337-347, doi:310.1016/j.epsl.2011.1001.1013.
 1178 Straub, S.M., Gomez-Tuena, A., Zellmer, G.F., Espinasa-Perena, R., Stuart, F.M., Cai, Y.,
 1179 Langmuir, C.H., Martin-Del Pozzo, A., Mesko, G.T., 2013a. The processes of melt
 1180 differentiation in arc volcanic rocks: Insights from OIB-type arc magmas in the central
 1181 Mexican Volcanic Belt. *J Petrol* 54, , 665-701, doi:610.1093/petrology/egs1081.
 1182 Straub, S.M., Gomez-Tuena, A., Zellmer, G.F., Espinasa-Perena, R., Stuart, F.M., Cai, Y.,
 1183 Langmuir, C.H., Martin-Del Pozzo, A., Mesko, G.T., 2013b. The processes of melt
 1184 differentiation in arc volcanic rock: Insights from OIB-type arc magmas in the central Mexican
 1185 Volcanic Belt: reply to a critical comment by Claus Siebe (2013). *J Petrol* 54, 1551-1554,
 1186 doi:1510.1093/petrology/egt1021
 1187 Straub, S.M., LaGatta, A.B., Martin-Del Pozzo, A.L., Langmuir, C.H., 2008. Evidence from high Ni
 1188 olivines for a hybridized peridotite/pyroxenite source for orogenic andesites from the central
 1189 Mexican Volcanic Belt. *Geochim Geophys Geosys* 9, Q03007, doi:03010.01029/02007GC001583.
 1190 Straub, S.M., Zellmer, G.F., 2012. Volcanic Arcs as Archives of Plate Tectonic Change. *Gondwana*
 1191 *Res* 21, 495-516, doi:410.1016/j.gr.2011.1010.1006
 1192 Straub, S.M., Zellmer, G.F., Gómez-Tuena, A., Espinasa-Perena, R., Martin-Del Pozzo, A.L.,
 1193 Stuart, F.M., Langmuir, C.H., 2014. A genetic link between silicic slab components and calc-
 1194 alkaline arc volcanism in central Mexico in: Gomez-Tuena, A., Straub, S.M., Zellmer, G.F.

1195 (Eds.), *Orogenic Andesites and Crustal Growth* Geological Society London Special
 1196 Publication, pp. 31-64, doi 10.1144/SP1385.1114.
 1197 Sun, S.S., McDonough, W.F., 1989. Chemical and isotopic systematics of oceanic basalts:
 1198 implications for mantle composition and processes, in: Saunders, A.D., Norry, M.J. (Eds.),
 1199 *Magmatism in the Ocean Basins*. Geol Soc Spec Publ Blackwell Scientific Publ, Oxford etc, pp.
 1200 313-345.
 1201 Tatsumi, Y., Eggins, E., 1995. *Subduction Zone Magmatism*. Blackwell Science, Cambridge MA.
 1202 Taylor, S.R., 1967. The origin and growth of continents. *Tectonophysics* 4, 17-34.
 1203 Tera, F., Brown, L., Morris, J., Sacks, I.S., 1986. Sediment incorporation in island-arc magmas:
 1204 Inferences from ¹⁰Be. *Geochim Cosmochim Acta* 50, 535-550.
 1205 Todt, W., Cliff, R.A., Hanser, A., Hofmann, A.W., 1996. Evaluation of a ²⁰²Pb-²⁰⁵Pb double-spike
 1206 for high-precision lead isotope analysis; in: Basu, A., Hart, S.R. (Eds.), *Earth Processes:*
 1207 *Reading the Isotopic Code*. AGU, Washington DC, pp. 429-437.
 1208 Tonarini, S., Leeman, W.P., Leat, P.T., 2011. Subduction erosion of forearc mantle wedge
 1209 implicated in the genesis of the South Sandwich Island (SSI) arc: Evidence from boron isotope
 1210 systematics. *Earth Planet Sci Lett* 301, 275–284, doi:210.1016/j.epsl.2010.1011.1008.
 1211 Vannucchi, P., Ranero, C.R., Galeotti, S., Straub, S.M., Scholl, D.W., McDougall-Ried, K., 2003.
 1212 Fast rates of subduction erosion along the Costa Rica Pacific margin: Implications for
 1213 nonsteady rates of crustal recycling at subduction zones. *J Geophys Res* 108, 2511,
 1214 2510.1029/2002JB002207.
 1215 Verma, S.P., 1999a. Geochemistry of evolved magmas and their relationship to subduction-
 1216 unrelated mafic volcanism at the volcanic front of the central Mexican Volcanic Belts. *J*
 1217 *Volcanol Geotherm Res* 93, 151-171.
 1218 Verma, S.P., 1999b. Geochemistry of the subducting Cocos plate and the origin of subduction-
 1219 unrelated mafic volcanism at the volcanic front of the central Mexican Volcanic Belt, in:
 1220 Delgado-Granados, H., Aguirre-Diaz, G., Stock, J.M. (Eds.), *Cenozoic Tectonics and Volcanism*
 1221 *at the volcanic front of the central Mexican Volcanic Belt*, pp. 1-28.
 1222 Vervoort, J.D., Plank, T., Prytulak, J., 2011. The Hf–Nd isotopic composition of marine sediments.
 1223 *Geochimica et Cosmochimica Acta* 75, 5903-5926, doi:5910.1016/j.gca.2011.5907.5046.
 1224 Wallace, P.J., Carmichael, I.S.E., 1999. Quaternary volcanism near the Valley of Mexico:
 1225 implications for subduction zone magmatism and the effects of crustal thickness variations on
 1226 primitive magma compositions. *Contrib Mineral Petrol* 135, 291-314.
 1227 Watkins, J.S., McMillen, K.J., Bachman, S.B., Shipley, T.H., Moore, J.C., Angevine, C., 1981.
 1228 *Tectonic synthesis Leg 66: Transect and vicinity*, in: Watkins, J.S., Moore, J.C. (Eds.), *DSDP Leg*
 1229 *66 Report*. US Gov Printing Office, Washington, pp. 837-849.
 1230 Watkins, J.S., Moore, J.C., 1981. Introduction: Scientific objectives and explanatory notes, Initial
 1231 Reports DSDP 66. US Govt Printing Office, Washington.
 1232

11. FIGURE CAPTIONS

Figure 1: Plate tectonic setting of the Trans-Mexican Volcanic Belt (MVB). **a.** Locations of DSDP/ODP/IODP drill sites samples on Pacific Plate (MORB glasses) and Cocos Plate (sediment, continental basement), and crust outcrops and xenoliths within and south of the MVB. Numbers in brackets next to IODP drill sites are basement ages in million years. Piston corer locations from Cai et al. (2014). Basemap from GeoMappApp (2014). **b.** Trans-Mexican Volcanic Belt (grey shaded) with principal Quaternary volcanoes redrawn from Blatter et al. (2001). Slab contours after Pardo and Suarez (1995). Locations of crustal materials are those of Gómez-Tuena et al. (2003, Palma Sola xenoliths), Martínez-Serrano et al. (2004, Nevado de Toluca xenoliths), Schaaf et al. (2005, Popocatepetl xenoliths), Gómez-Tuena et al. (2008, Chalcatzingo xenolith), Ortega-Gutiérrez et al. (2011, Puente Negro xenoliths), Hernández-Pineda et al. (2011, Eocene Acapulco intrusion), Pérez-Gutiérrez et al. (2009, Mesozoic Xolapa migmatites) and Ortega-Gutiérrez et al. (2014, Valle Santiago xenoliths). NDT – Nevado de Toluca, POP – Popocatepetl, EPR – East Pacific Rise, RFZ – Rivera Fracture Zone, MC – Mexico City, TFZ – Tamayo Fracture Zone. **c.** NE-SW cross section of Mexican continental slope and trench with incoming Cocos plate drilled during DSDP Leg 66, redrawn from Watkins et al. (1981). Continental basement was drilled at Sites 493 (granodiorite) and 489 (B-biotite gneiss). Trench sediment was analyzed at Sites 488 and 487 (Cai et al., 2014; LaGatta, 2003; Plank, 2014; Plank and Langmuir, 1998; Verma, 1999b), and oceanic basement at Site 487 (Cai et al., 2014, this study; Verma, 1999b).

Figure 2: Study area in the central Mexican Volcanic Belt. Monogenetic volcanoes (small open circles) of the Sierra Chichinautzin Volcanic Field are flanked by Quaternary composite volcanoes Nevado de Toluca and Popocatepetl-Iztaccihuatl. Large symbols denote samples with olivines analyzed for both $^3\text{He}/^4\text{He}$ and $\delta^{18}\text{O}$. Location of most mantle-like magmas ('Old Texcal Flow') is indicated, as well as location of high-La volcanic rocks (St. Cruz, Tuxtepec and Yecahuazac Cone). CV – City of Cuernavaca, TL City of Toluca

Figure 3: Multi-element diagram of incompatible trace elements of central MVB magmas normalized to primitive mantle of McDonough and Sun (1995). For clarity, only magmas with high $^3\text{He}/^4\text{He}$ and high $\delta^{18}\text{O}$ are shown. **a.** Thick black line denotes the 'Old Texcal Flow' which is least influenced by slab and closely resembles a ~3.5% melt from primitive mantle (Straub et al., 2013a, 2013b). While per definition a high-Nb basalt (Nb=18 ppm), it has no end member character and is intermediate to calc-alkaline and high-Nb series. **b.** MVB magmas compared to melts from residual mantle after 3.5 to 10% melt extraction from a primitive mantle (which produced the Old Texcal Flow after minor subduction modification). Residual mantle modeled from primitive mantle McDonough and Sun (1995) and partition coefficients from Donnelly et al. (2004). Mantle depletion by melting is so efficient that the slab flux either strongly influences (MREE) or controls (LREE and more incompatible elements) the arc budgets of elements more incompatible than Ho. Only Ti and rare earth elements Ho to Lu remain mantle-controlled by mantle. See also Straub et al. (2014).

Figure 4: $^3\text{He}/^4\text{He}$ vs $\delta^{18}\text{O}$ of olivine phenocrysts in central MVB volcanic rocks. $\delta^{18}\text{O}$ recalculated to ratios in equilibrium melt [$\delta^{18}\text{O}_{\text{melt}} = \delta^{18}\text{O}_{\text{oliv}} + 0.088 * \text{SiO}_2 - 3.57$ after Bindeman (2008)]. $^3\text{He}/^4\text{He}$ of olivines are from Straub et al. (2011b). $^3\text{He}/^4\text{He}$ in MORB and continental crust from Farley et al. (1998) and O'Nions and Oxburgh (1988); $\delta^{18}\text{O}$ in mantle rocks from Bindeman (2008). Host magmas are basalts to andesites with up to 61 wt% SiO_2 .

Figure 5: $^{87}\text{Sr}/^{86}\text{Sr}$ vs $^{143}\text{Nd}/^{144}\text{Nd}$ of volcanic rocks and various crustal materials (Cenozoic MORB, trench sediment, continental basement). See Figure 1 for sample locations. Quaternary MORB is from the East Pacific Rise (PetDB, 2011). Large symbols denote volcanic rocks with olivines analyzed for $^3\text{He}/^4\text{He}$ and $\delta^{18}\text{O}$. Thick grey lines are simple mixing curves between AOC, mantle wedge (which have similar $^{87}\text{Sr}/^{86}\text{Sr}$ and Sr/Nd) and trench sediment (see text for discussion). The biotite gneiss of DSDP Site 489 is marked with a 'B'. Inset identifies the Old Texcal Flow and illustrates differences between calc-alkaline, high-La and Nb-rich magmas. For data sources see text.

Figure 6: **a.** $^{143}\text{Nd}/^{144}\text{Nd}$ vs. $^{176}\text{Hf}/^{177}\text{Hf}$, and **b.** $^{176}\text{Hf}/^{177}\text{Hf}$ vs. Nd/Hf of central MVB magmas and crustal materials (MORB, trench sediment, continental basement). See Figure 5 for symbols. Thick grey lines are simple mixing curves between AOC and trench sediment. Note that a mantle component would not affect the curvature of the mixing line, since mantle has similar $\text{Nd}/\text{Hf} \sim 4$ (as well as Nd and Hf isotopic ratios) as the AOC. Mixing models must match arc data in both diagrams to be valid. The trench sediment fails as crust end member, while the offshore/Acapulco granodiorite lie in line with the AOC and compositions. Inset identifies the Old Texcal Flow and illustrates differences between calc-alkaline, high-La and Nb-rich magmas. For data sources see text.

Figure 7: **a.** $^{207}\text{Pb}/^{204}\text{Pb}$ vs. $^{206}\text{Pb}/^{204}\text{Pb}$, and **b.** $^{208}\text{Pb}/^{204}\text{Pb}$ vs. $^{206}\text{Pb}/^{204}\text{Pb}$ of central MVB magmas and crustal materials (MORB, trench sediment, continental basement). See Figure 5 for symbols. The thick grey line is a mixing curve (which are linear in Pb isotope space) through the central MVB magmas which are aligned with slab and mantle materials. The Cenozoic AOC (average ~ 18.2) fits much better as unradiogenic end member of the arc array than the more variable zero-age Quaternary MORB from the East Pacific Rise. Inset identifies the Old Texcal Flow and illustrates differences between calc-alkaline, high-La and Nb-rich magmas. For data sources see text.

Figure 8: Central MVB magmas: **a.** Bulk rock $^{143}\text{Nd}/^{144}\text{Nd}$ vs SiO_2 wt%. **b.** $^3\text{He}/^4\text{He}$ (olivine) vs SiO_2 wt% (bulk rock) with mixing curves from Straub et al. (2014). **c.** $\delta^{18}\text{O}$ (olivine) vs SiO_2 wt% (bulk rock), and **d.** $\delta^{18}\text{O}_{\text{melt}}$ [calculated from olivine after Bindeman (2008): $\delta^{18}\text{O}_{\text{melt}} = \delta^{18}\text{O}_{\text{oliv}} + 0.088 * \text{SiO}_2 (\text{wt}\%) - 3.57$] vs SiO_2 wt% (bulk rock). MORB field and fractional crystallization trajectory after Bindeman (2008). Mixing curves calculated with a crustal component $\text{SiO}_2 = 69$ wt% and $\delta^{18}\text{O} = 8\text{--}12$ ‰, and a mantle melt of $\text{SiO}_2 = 49$ wt% and $\delta^{18}\text{O} = 5.8$ ‰, respectively. See text for discussion.

Figure 9: $\delta^{18}\text{O}_{\text{melt}}$ vs. average fosterite of cores of olivine phenocrysts. Olivine concentrations are from Straub et al. (2011b; 2013a, this study; 2008). The $\delta^{18}\text{O}$ of continental crust is after Bindeman (2008).

Figure 10: Nd-Hf isotope and trace element mixing models. Valid models require mixing curves to pass through arc data in both the $^{143}\text{Nd}/^{144}\text{Nd}$ vs $^{176}\text{Hf}/^{177}\text{Hf}$ and Nd/Hf vs $^{176}\text{Hf}/^{177}\text{Hf}$ space. The models first calculate a 'bulk slab component' (AOC and bulk trench sediment, or AOC and granodiorite) shown as thick lines with 10% increments. The bulk slab component then mixes with the mantle wedge, shown as lines with only two tick marks (1% and 10%) for clarity (dashed - denotes curve for Nb-rich magmas). for . **a.-b.** Mixing between AOC and bulk trench sediment with preferential release of Hf from sediment by a factor of 7. **c.-d.** Mixing between AOC and bulk trench sediment with preferential release of Nd from AOC by a factor of 7. Either model produces misfits in the Nd/Hf vs $^{176}\text{Hf}/^{177}\text{Hf}$ space (except for the high-La basalts). **e.-f.** Mixing between AOC and granodiorite that have similar Nd/Hf ratios. Calc-alkaline and Nb-rich magmas require slightly different crustal and mantle end members in isotope space. Mixing model assumes primitive background mantle (Nd/Hf= 4.4) for Nb-rich magmas, and a residual mantle after by 5% melt extraction for calc-alkaline series (Nd/Hf=3.9). For details see text.

Figure 11: Idealized $^{87}\text{Sr}/^{86}\text{Sr}$ vs $^{143}\text{Nd}/^{144}\text{Nd}$ mixing model for calc-alkaline/high-La and Nb-rich magmas, respectively, with AOC, granodiorite and mantle wedge as end members. The models first calculate a 'bulk slab component'(AOC and bulk trench sediment, or AOC and granodiorite) which are shown as thick lines with 10% increments. The bulk slab component then mixes with the mantle wedge, shown as lines with only two tick marks (1% and 10%) for clarity (dashed - denotes curve for Nb-rich magmas). A successful model for the calc-alkaline series requires a component with increased $^{87}\text{Sr}/^{86}\text{Sr}$, depicted here to derive from subducted AOC.

Figure 12: Idealized $^{208}\text{Pb}/^{204}\text{Pb}$ vs. $^{206}\text{Pb}/^{204}\text{Pb}$ mixing model for a. calc-alkaline/high-La magmas, and b. Nb-rich magmas. The models first calculate a 'bulk slab component'(AOC and bulk trench sediment, or AOC and granodiorite) which are shown as thick lines with 10% increments (dashed - denotes curve for Nb-rich magmas in panel b). The bulk slab component then mixes with the mantle wedge, shown as lines with only two tick marks (1% and 10%) for clarity (dashed - denotes curve for Nb-rich magmas).

Figure 13: **a.** Percentage of slab-derived Pb in arc magmas vs. $^{206}\text{Pb}/^{208}\text{Pb}$. **b.** Percentage of slab-derived Sr in arc magmas vs. $^{87}\text{Sr}/^{86}\text{Sr}$. For calculation of slab-derived percentages see text. **c.** Percentage of slab-derived Nd in arc magmas vs. $^{143}\text{Nd}/^{144}\text{Nd}$. **d.** Percentage of slab-derived Hf in arc magmas vs. $^{176}\text{Hf}/^{177}\text{Hf}$.

Figure 14: Cartoon of central MVB subduction setting. Thermal structure model assumes mantle potential temperature of 1450°C and temperatures of ~700-800°C at about 110 km beneath the central MVB arc front, estimated from P-wave seismic tomography (Manea and Manea, 2011).

Slab surface temperatures remains below sediment solidus ($\geq 1050^{\circ}\text{C}$, Behn et al., 2011)), but are conducive to the formation of thermochemical instabilities at the slab–mantle interface.

Figure 15: **a.-b.** Th/La *vs.* $^{143}\text{Nd}/^{144}\text{Nd}$, and **c.-d.** Nb/Ta *vs.* $^{143}\text{Nd}/^{144}\text{Nd}$ and mixing models for MVB magmas and their source components. Stippled lines outlines the range of the Acapulco/offshore granodiorites. The mixing models first calculate a 'bulk slab component' from AOC and eroded crust (thick lines with 10% increments). The bulk slab component then mixes with the mantle wedge, shown as lines with only two tick marks (1% and 10%) for clarity (dashed - denotes curve for Nb-rich magmas). Averages of major Earth reservoirs (right panels) are compiled from Plank (2004), McDonough and Sun (1995), Sun and McDonough (1989), Pfänder et al. (2007), and Muenker et al. (2003).

Figure 16: Nb (ppm) *vs* Nb/Ta of central MVB arc volcanic rocks with range of MORB from Niu and Batiza (1997). Stippled lines mark average of Old Texcal Flow (proxy to subarc mantle wedge prior to subduction modification).

Table 1: Average percentages of slab contributions of Pb, Sr, Nd and Hf to calc-alkaline, high-La and Nb-rich magmas from trace element inversion.

| | Sr | Pb | Nd | Hf |
|-----------------------|--------|--------|--------|--------|
| calc-alkaline magmas | 87±4% | 89±6% | 74±8% | 69±9% |
| <i>from mantle</i> | ~13% | ~11% | ~26% | ~31% |
| | | | | |
| high-La series magmas | 95±2% | 96±2% | 93±3% | 73±7% |
| <i>from mantle</i> | ~5% | ~4% | ~7% | ~27% |
| | | | | |
| Nb-rich magmas | 49±10% | 59±18% | 47±16% | 44±13% |
| <i>from mantle</i> | ~51% | ~41% | ~53% | ~56% |

Table 2: Source components used for $^{143}\text{Nd}/^{143}\text{Nd}$ vs. $^{176}\text{Hf}/^{177}\text{Hf}$ isotope mixing models.

| | $^{87}\text{Sr}/^{86}\text{Sr}$ | $^{143}\text{Nd}/^{144}\text{Nd}$ | $^{206}\text{Pb}/^{208}\text{Pb}$ | $^{208}\text{Pb}/^{208}\text{Pb}$ | $^{176}\text{Hf}/^{177}\text{Hf}$ | Pb ppm | Sr ppm | Nd ppm | Hf ppm | Sr/Nd | Nd/Hf | Data Sources |
|---------------------------------------|---------------------------------|-----------------------------------|-----------------------------------|-----------------------------------|-----------------------------------|-----------|------------------|-----------|-----------|-------|-------|--|
| Cenozoic MORB (AOC) | 0.70350 | 0.51319 | 18.20 | 37.71 | 0.28321 | 0.62 | 123 ^a | 10.28 | 2.57 | 11.9 | 4.00 | this study |
| Bulk trench sediment | 0.70825 | 0.51253 | 18.64 | 38.34 | 0.28290 | 38.9 | 208 | 28.5 | 2.48 | 7.3 | 11.5 | (Cai et al., 2014; Plank, 2014) |
| Pelagic trench sediment | 0.70837 | 0.51253 | 18.51 | 38.19 | 0.28294 | 66.2 | 284 | 51.2 | 2.51 | 5.6 | 20.4 | (Cai et al., 2014; LaGatta, 2003; Verma, 1999b) |
| Terrigenous trench sediment | 0.70858 | 0.51248 | 18.84 | 38.62 | 0.28278 | 20.9 | 179 | 19.8 | 2.43 | 9.1 | 8.15 | (Cai et al., 2014; LaGatta, 2003; Verma, 1999b) |
| | | | | | | | | | | | | |
| <i>calc-alkaline/high-La series</i> | | | | | | | | | | | | |
| Background mantle wedge | 0.70307 | 0.51300 | 18.71 | 38.41 | 0.28306 | 0.076 | 7.8 | 0.63 | 0.164 | 12.3 | 3.86 | this study; residual of primitive mantle from McDonough and Sun (1995), after 3.5% melt extraction |
| Acapulco/offshore granodiorite | 0.70460 | 0.51273 | 18.8 | 38.64 | 0.28291 | 13.6 | 294 ^b | 32.8 | 5.70 | 9.0 | 5.75 | this study. |
| | | | | | | | | | | | | |
| <i>Nb-rich series</i> | | | | | | | | | | | | |
| Background mantle wedge | 0.70307 | 0.51300 | 18.71 | 38.41 | 0.28306 | 0.15 | 19.9 | 1.25 | 0.283 | 15.9 | 4.42 | this study; primitive mantle from McDonough and Sun (1995) |
| intraplate seamount | 0.70460 ^c | 0.51273 ^c | 18.8 ^c | 38.64 ^c | 0.2829 ^c | 1.2 | 270 | 21.2 | 4.2 | 12.8 | 5.0 | abundance data after Niu and Batiza (1997), Nb>10 ppm |

a Model in Figure 14, uses increased Sr abundances, by factor of 3 for calc-alkaline series (Sr= 368 ppm; Sr/Nd=36), and by a factor of 2.5 for the NEAB (Sr= 306 ppm; Sr/Nd= 30).

b Model in Figure 14, uses increased Sr abundances, by factor of 4 (Sr= 1177 ppm; Sr/Nd=36)

c Isotope ratios estimated from trend of Nb-rich magmas in Sr-Nd-Pb-Hf isotope space

Table 3. Average percentages of Pb, Sr, Nd and Hf contributed from the mantle and the different slab reservoirs obtained from isotope modeling.

| | Sr% | Pb% | Nd% | Hf% |
|-------------------------------------|-----|-----|-----|-----|
| Calc-alkaline/high-La series | | | | |
| <i>mantle</i> | 4 | 14 | 11 | 14 |
| <i>AOC</i> | 23 | 25 | 21 | 27 |
| <i>Granodiorite</i> | 73 | 61 | 68 | 59 |
| | | | | |
| Nb-rich magmas | | | | |
| <i>mantle</i> | 22 | 24 | 24 | 25 |
| <i>AOC</i> | 42 | 22 | 25 | 28 |
| <i>Seamount</i> | 37 | 54 | 51 | 46 |

Table 4: Source components used for Th/La vs. $^{143}\text{Nd}/^{144}\text{Nd}$ and Nb/Ta vs. $^{143}\text{Nd}/^{144}\text{Nd}$ mixing models.

| | $^{143}\text{Nd}/^{144}\text{Nd}$ | Th ppm | La ppm | Nb ppm | Ta ppm | Th/La | Nb/Ta | Data Sources |
|---------------------------------------|-----------------------------------|----------|-----------|-----------|-----------|-----------|-----------|--|
| Cenozoic MORB (AOC) | 0.51319 | 0.33 | 4.9 | 4.55 | 0.285 | 0.07 | 15.6 | this study |
| Bulk trench sediment | 0.51253 | 6.00 | 36.3 | 8.65 | 0.557 | 0.17 | 15.5 | (Cai et al., 2014; Plank, 2014) |
| Pelagic trench sediment | 0.51253 | 5.51 | 56.4 | 8.09 | 0.44 | 0.08 | 18.2 | (Cai et al., 2014; LaGatta, 2003; Verma, 1999b) |
| Terrigenous trench sediment | 0.51248 | 7.50 | 20.4 | 11.04 | 0.84 | 0.32 | 13.2 | (Cai et al., 2014; LaGatta, 2003; Verma, 1999b) |
| Acapulco/offshore granodiorite | 0.51270-0.51276 | 1.1-13.6 | 15.1-37.1 | 15.7-30.9 | 1.36-1.58 | 0.07-0.37 | 11.5-19.6 | this study. |
| | | | | | | | | |
| <i>calk-alkaline/high-La series</i> | | | | | | | | |
| Background mantle wedge | 0.51300 | 0.0011 | 0.105 | 0.02 | 0.0012 | 0.01 | 16.22 | this study; residual of primitive mantle from McDonough and Sun (1995), after 3.5% melt extraction |
| | | | | | | | | |
| <i>Nb-rich magmas</i> | | | | | | | | |
| Background mantle wedge | 0.51300 | 0.0795 | 0.648 | 0.6 | 0.037 | 0.12 | 16.22 | this study; primitive mantle from McDonough and Sun (1995) |

Figure

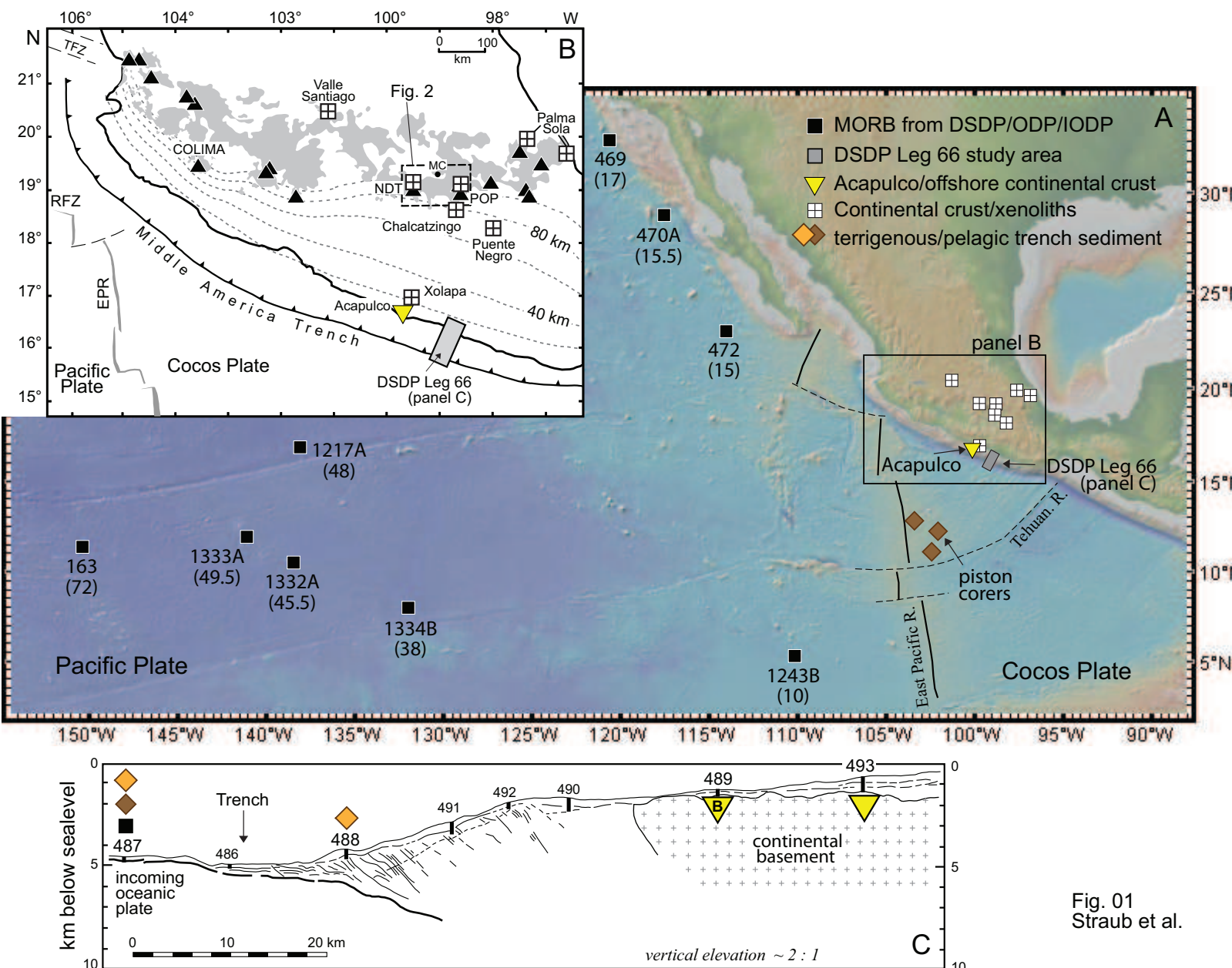


Fig. 01
Straub et al.

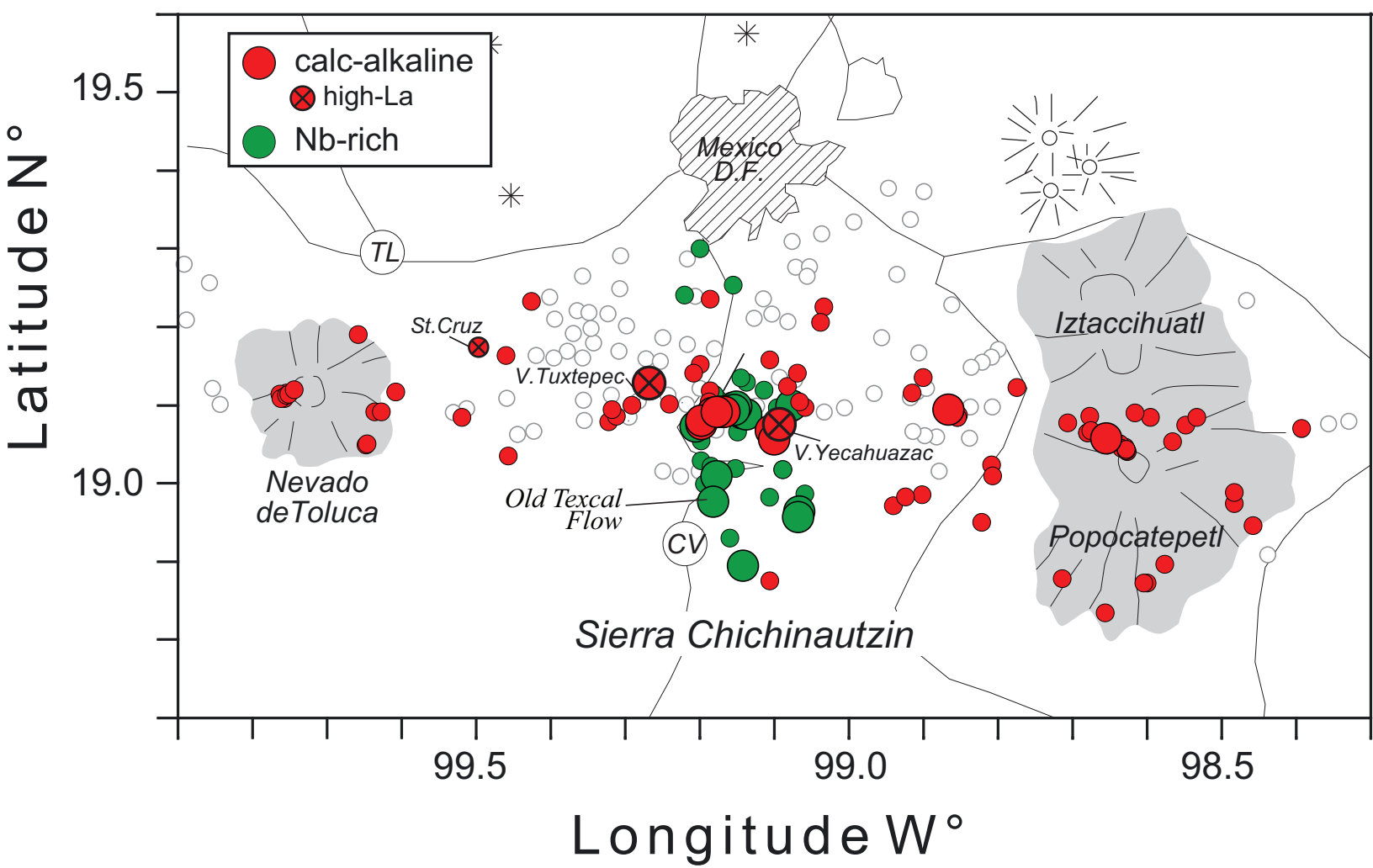


Fig. 02
Straub et al.

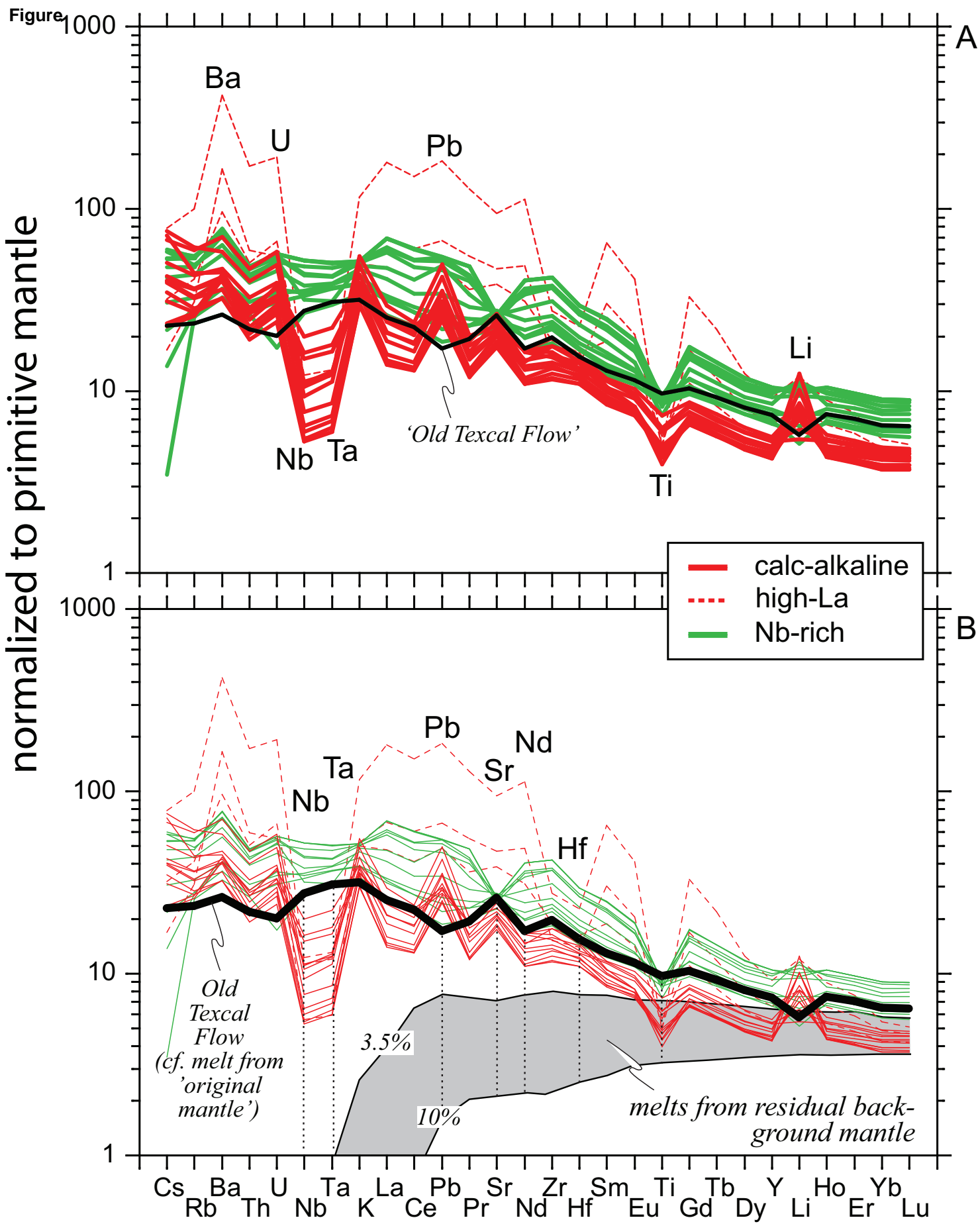
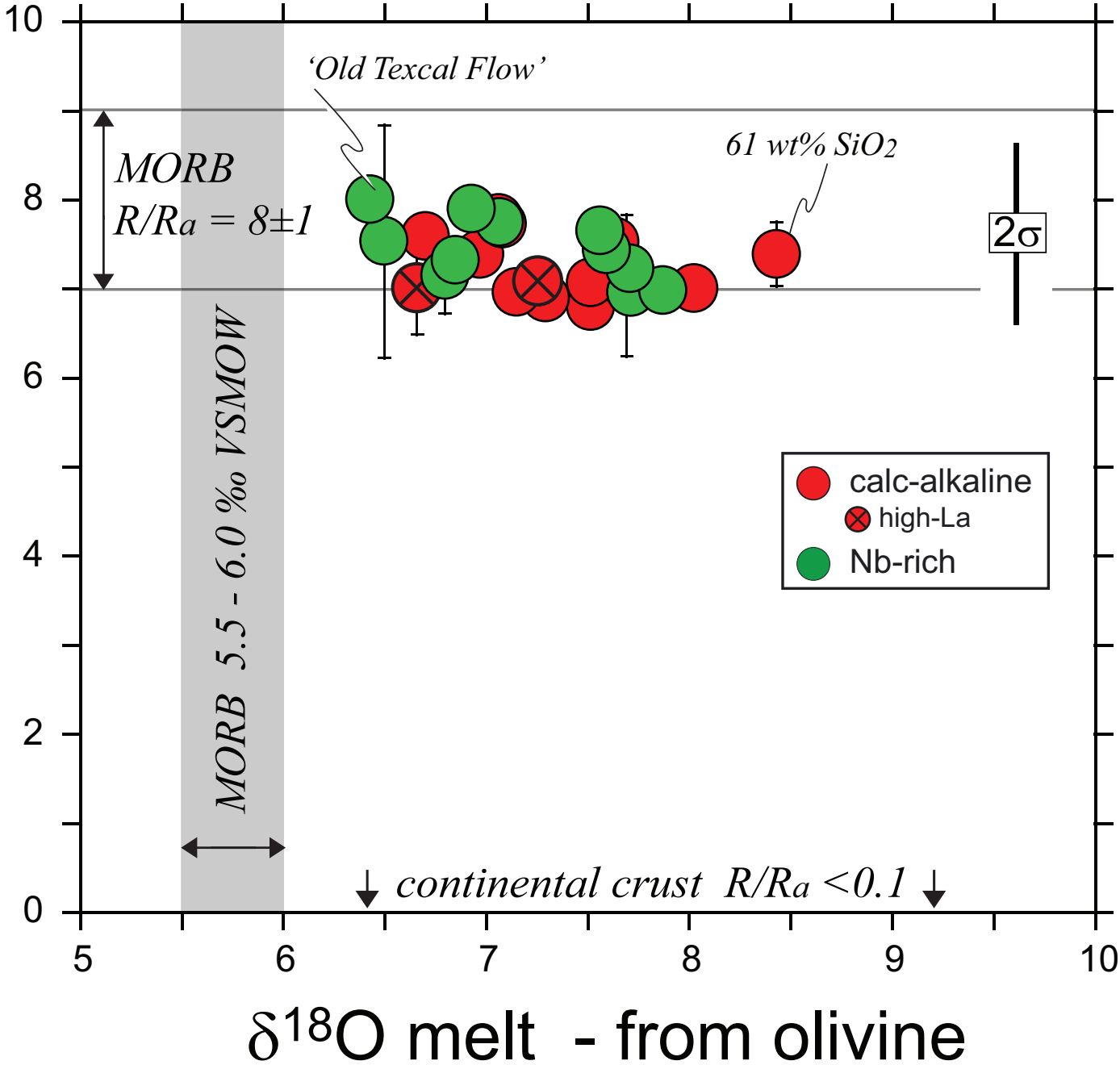


Fig. 03
Straub et al.

Figure

 $^3\text{He}/^4\text{He } R_a$ - from olivineFig. 04
Straub et al.

Figure

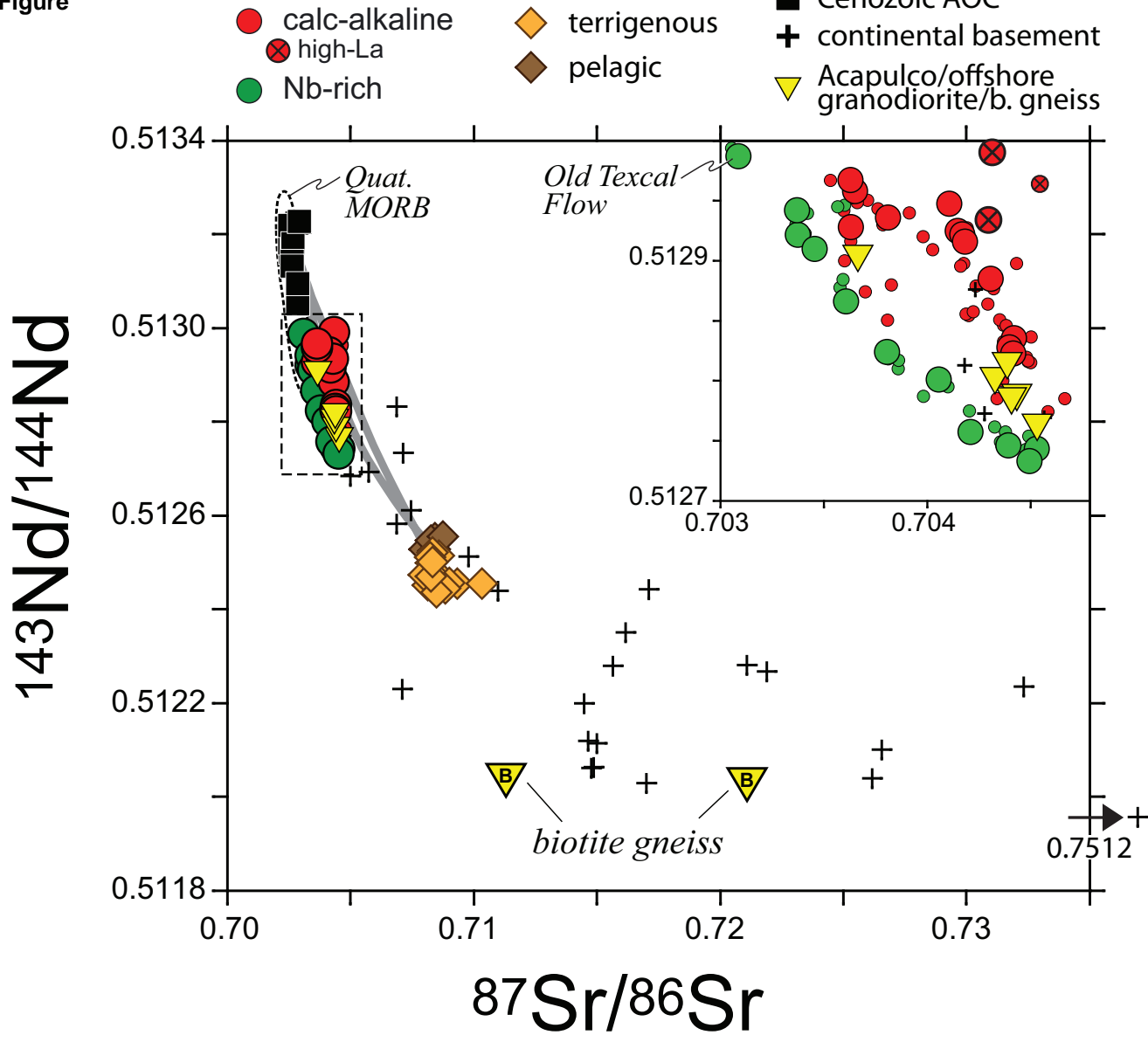
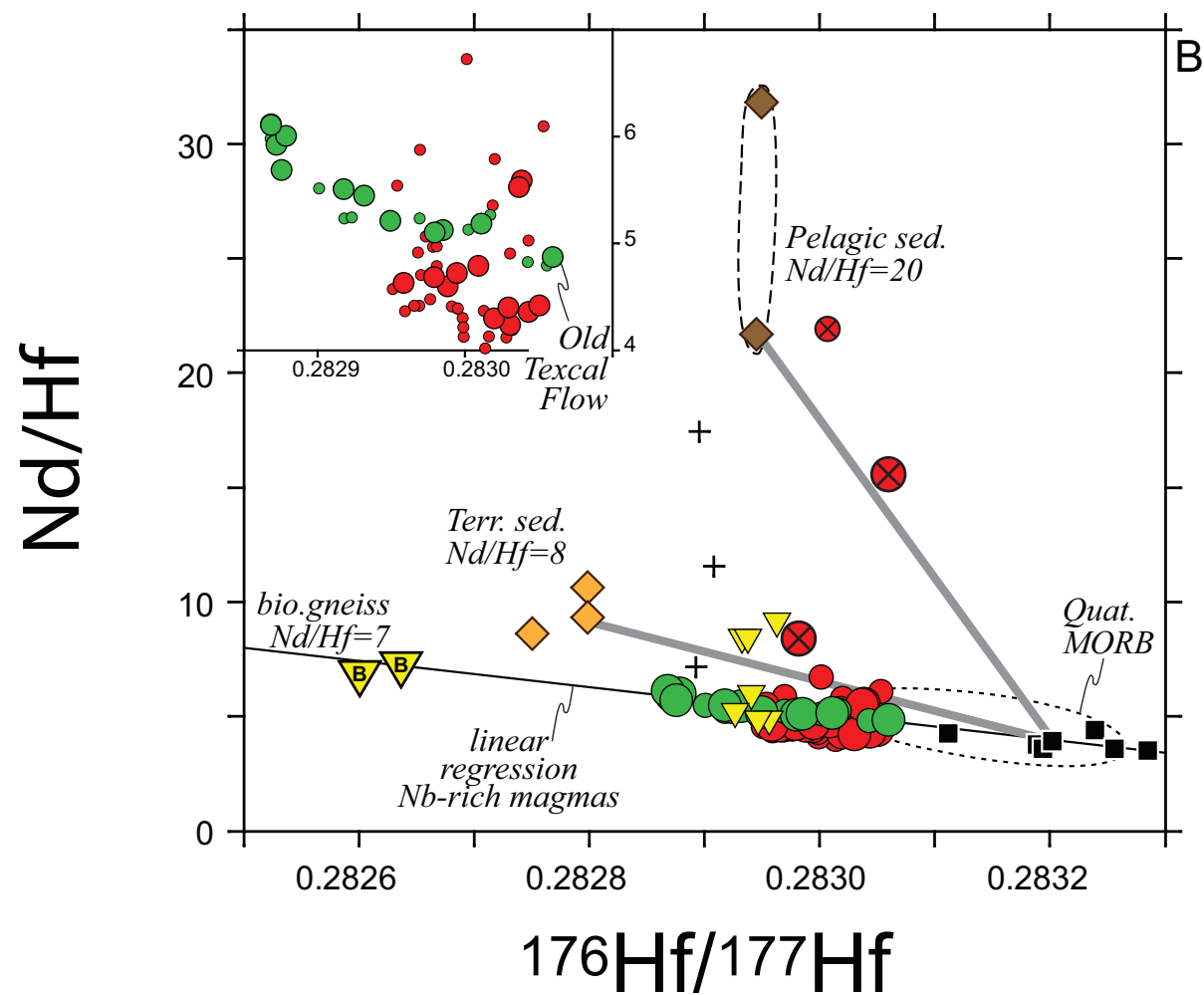
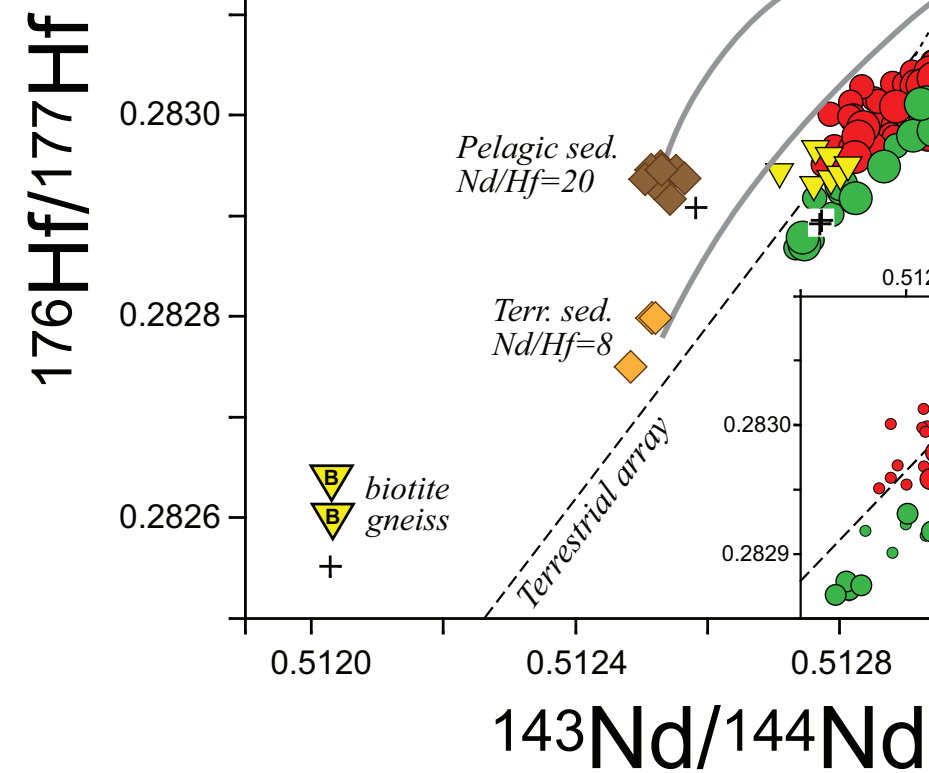
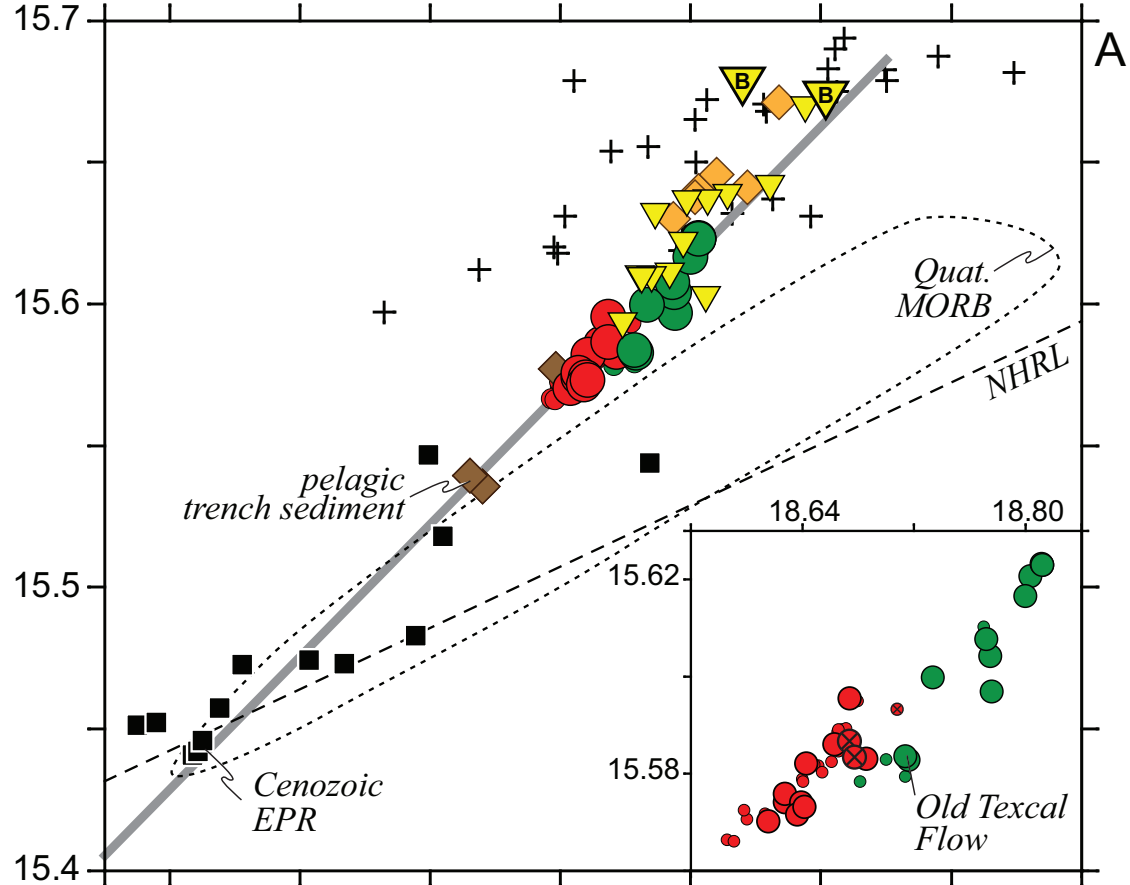
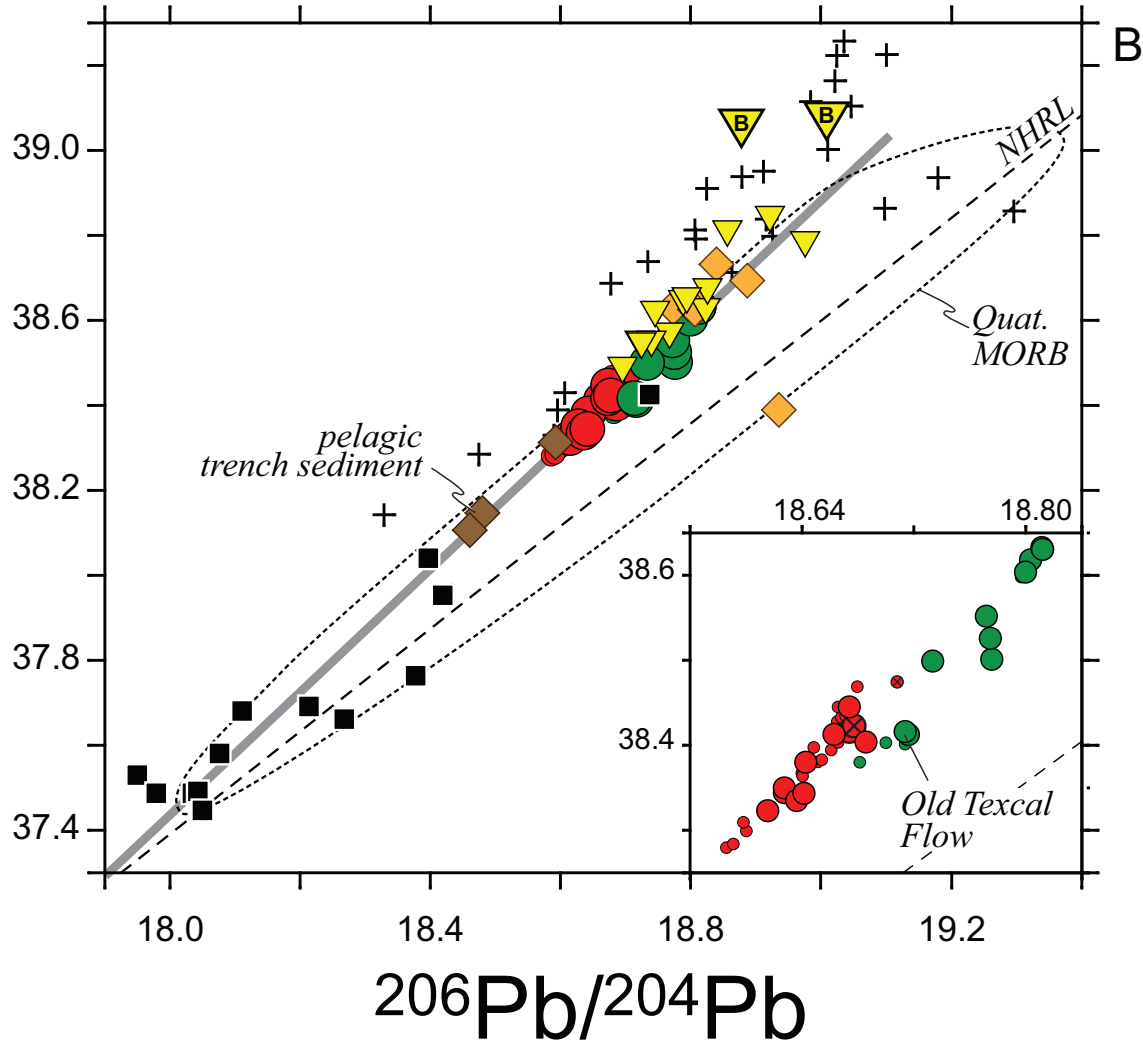


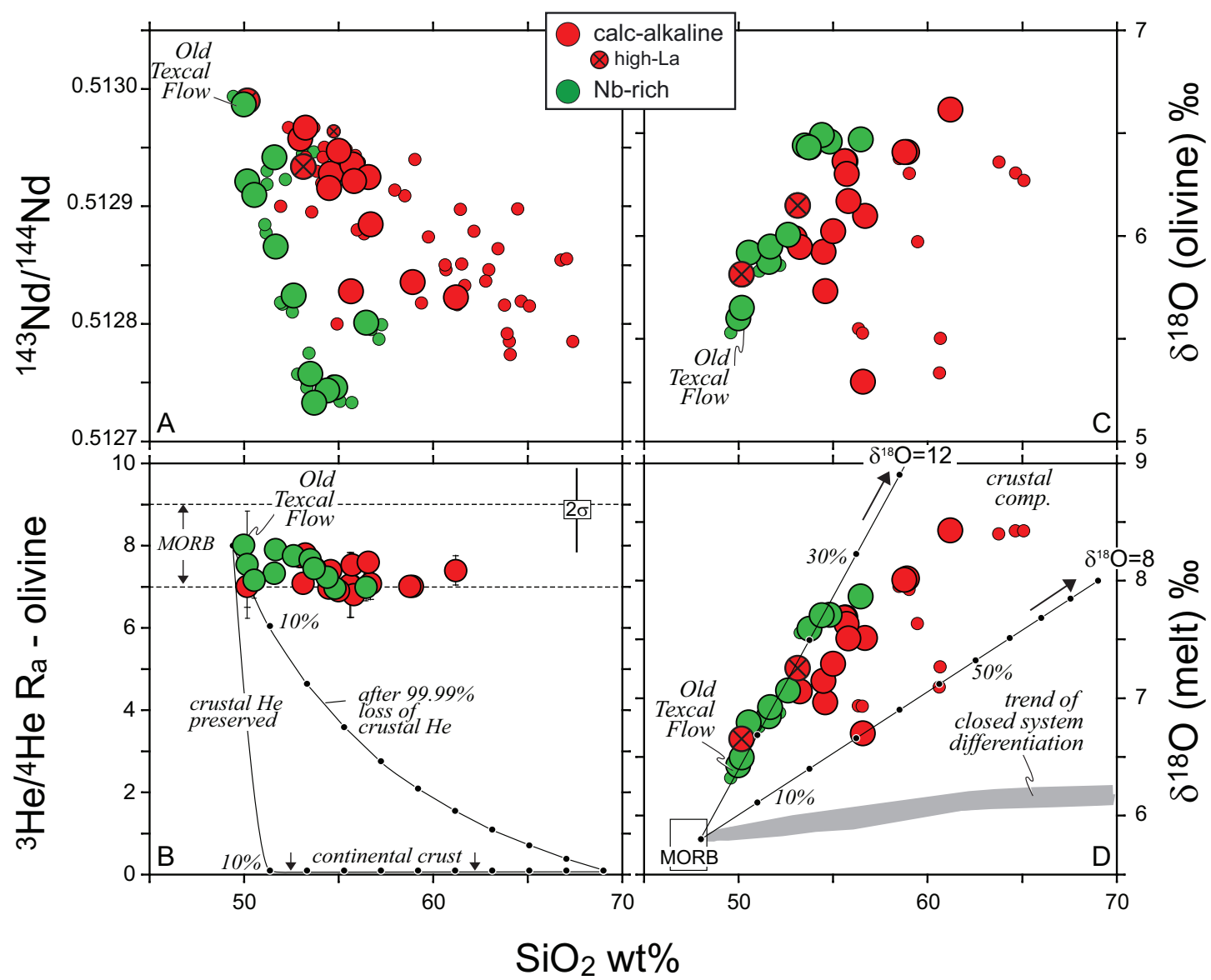
Fig. 05
Straub et al.

Fig. 06
Straub et al.

Figure

 $^{207}\text{Pb}/^{204}\text{Pb}$  $^{208}\text{Pb}/^{204}\text{Pb}$ Fig. 07
Straub et al.

Figure

Fig. 08
Straub et al.

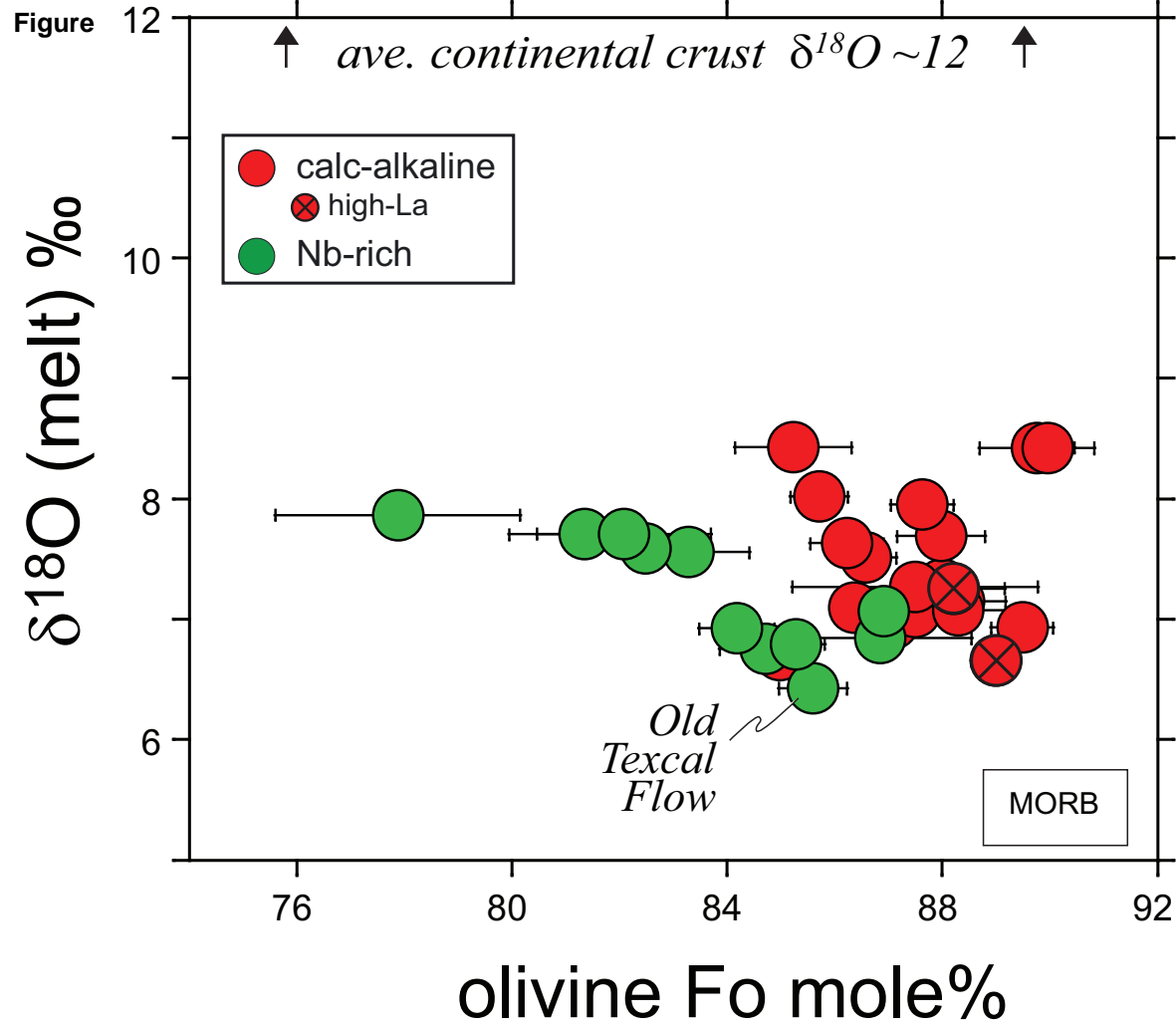


Fig. 09
Straub et al.

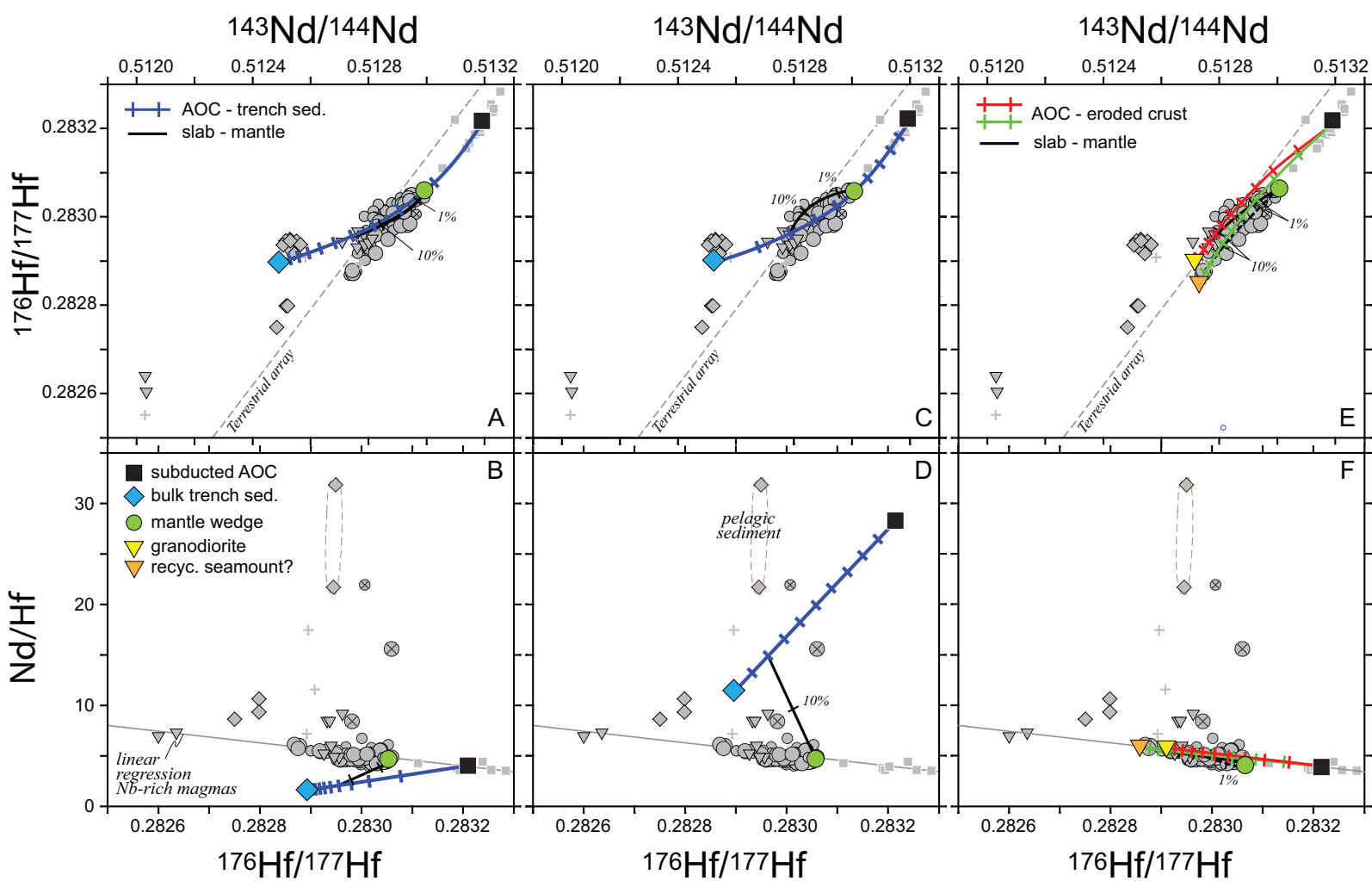


Fig. 10
Straub et al.

Figure

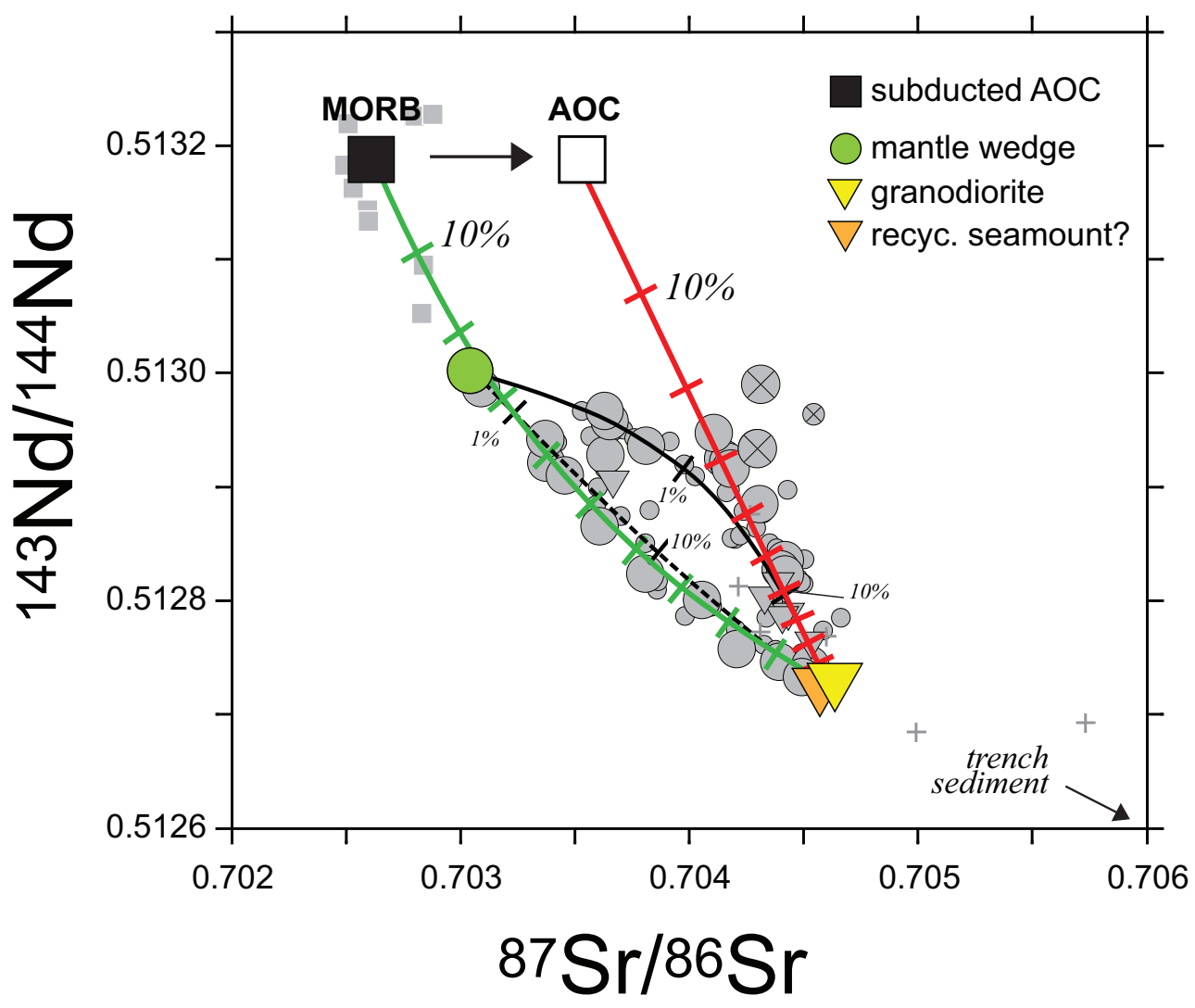


Fig. 11
Straub et al.

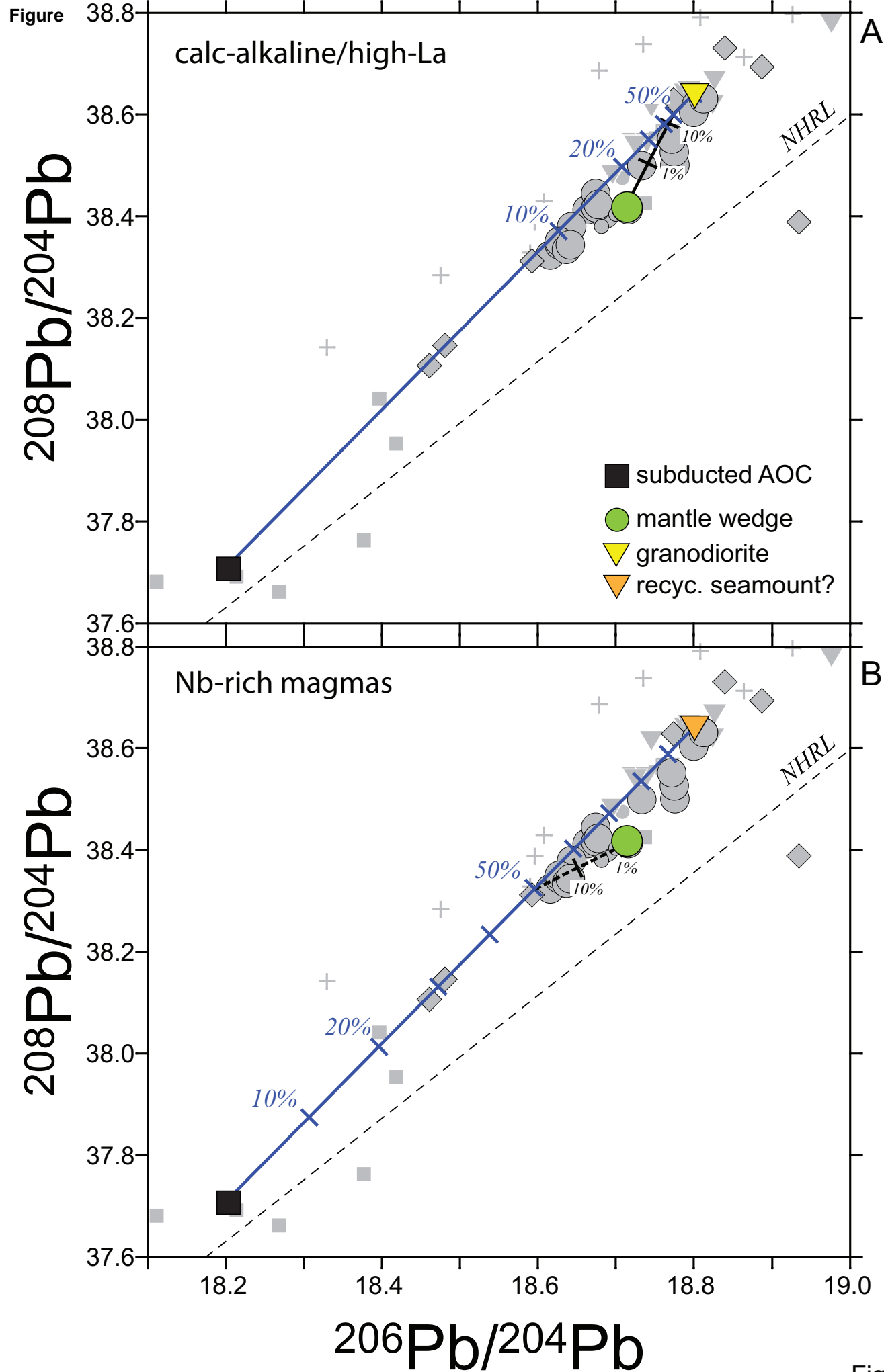


Fig. 12
Straub et al.

Figure

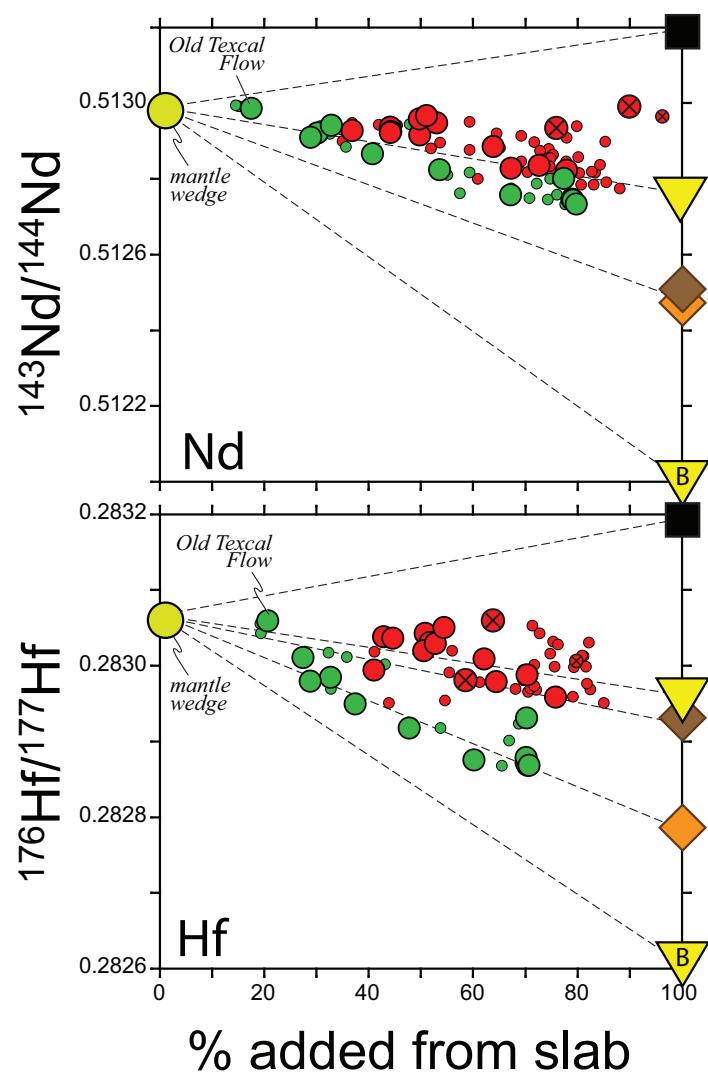
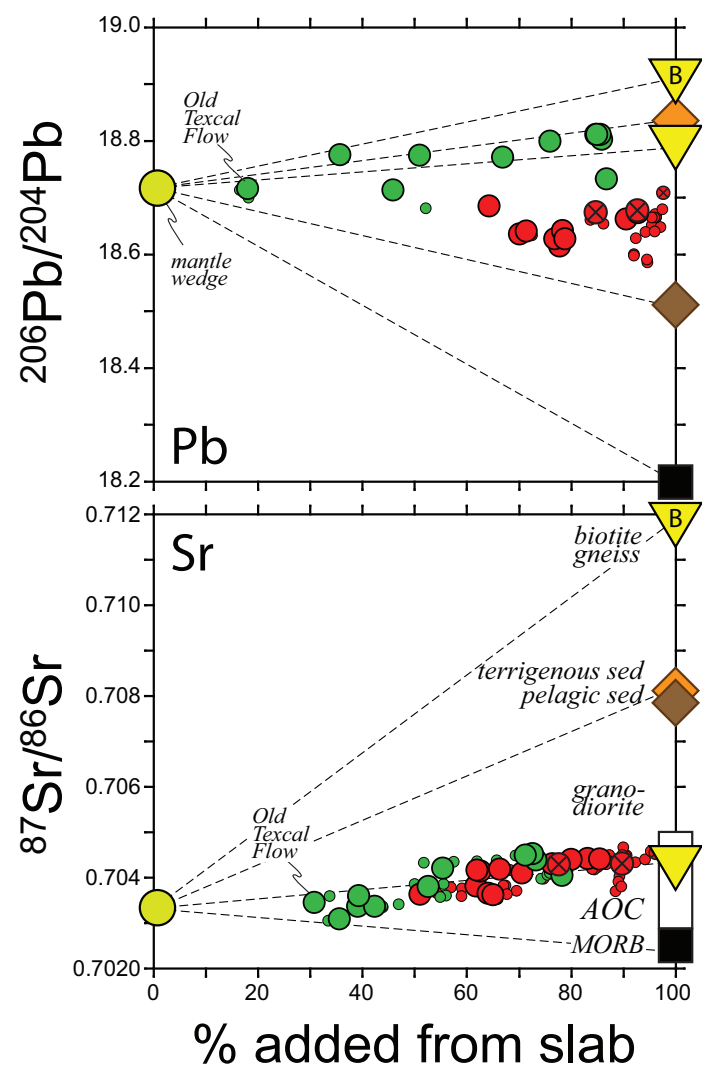


Fig. 13
Straub et al.

Figure

Depth (km below seafloor)

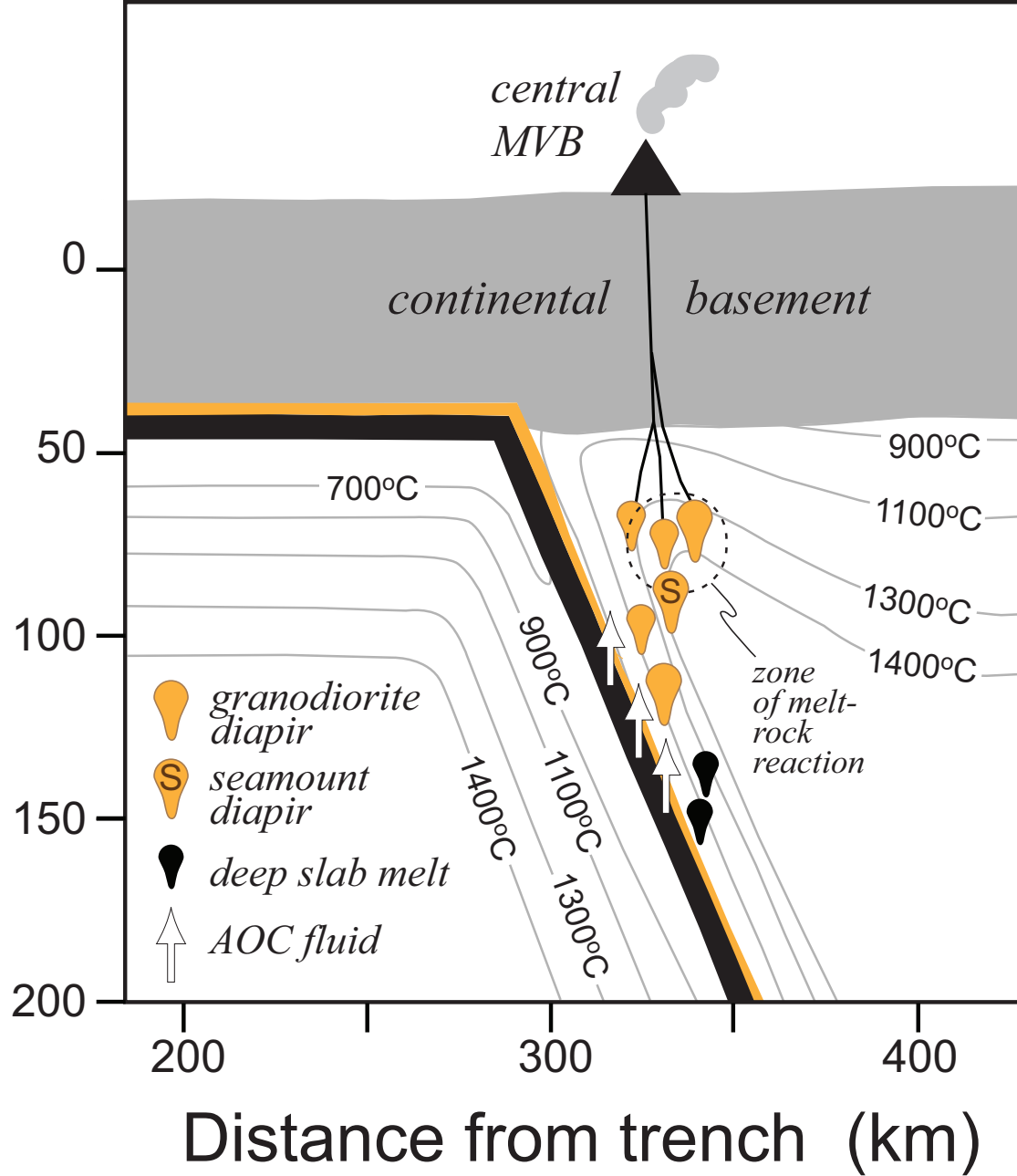
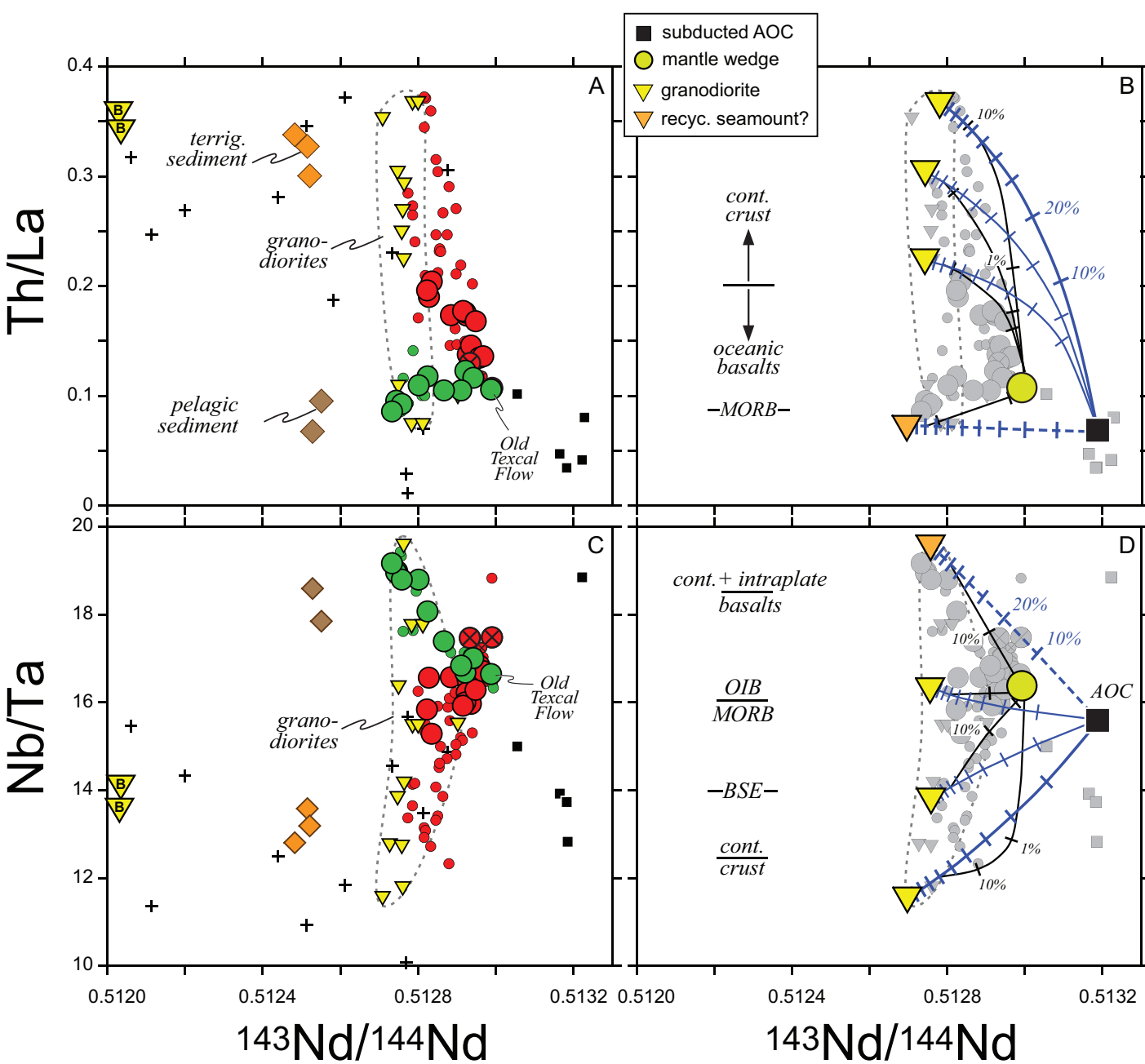


Fig. 14
Straub et al.

Figure

Fig. 15
Straub et al.

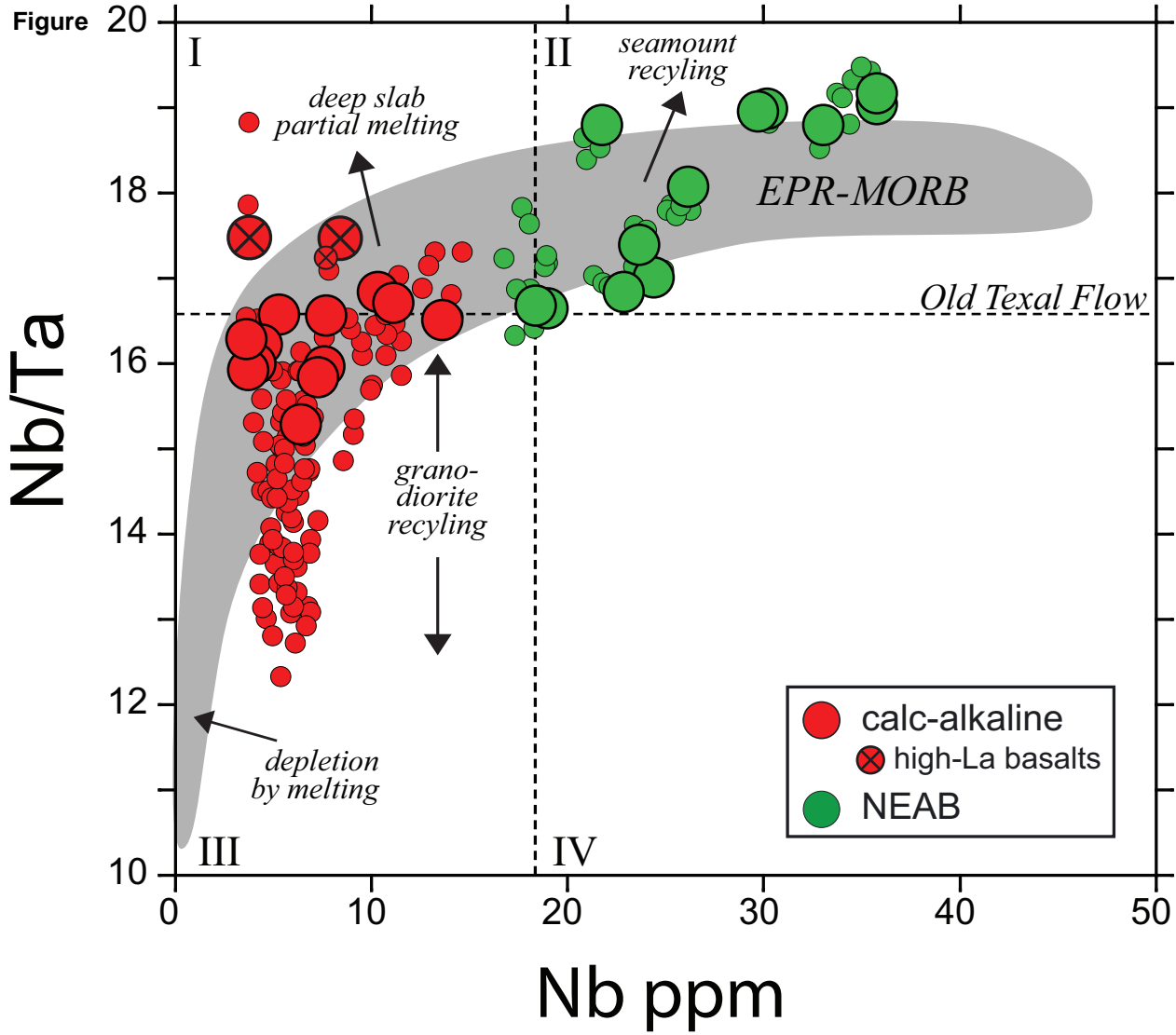


Fig. 16
Straub et al.

Electronic Annex

[Click here to download Electronic Annex: Appendix_A_B_rev2.pdf](#)

Electronic Annex

[Click here to download Electronic Annex: Appendix Table 1.xls](#)

Electronic Annex

[Click here to download Electronic Annex: Appendix Table 2.xls](#)

Electronic Annex

[Click here to download Electronic Annex: Appendix Table 3.xls](#)

Electronic Annex

[Click here to download Electronic Annex: Appendix Table 4.xls](#)

Electronic Annex

[Click here to download Electronic Annex: Appendix Table 5.xls](#)

Electronic Annex

[Click here to download Electronic Annex: Appendix Table 6.xls](#)

Electronic Annex

[Click here to download Electronic Annex: Appendix Table 7.xls](#)

Electronic Annex

[Click here to download Electronic Annex: Appendix Table 8.xls](#)

Electronic Annex

[Click here to download Electronic Annex: Appendix Table 9.xls](#)

Electronic Annex

[Click here to download Electronic Annex: Appendix_Table 10.xls](#)